

S.-J. Kim · G.M. Flato · G.J. Boer

A coupled climate model simulation of the Last Glacial Maximum, Part 2: approach to equilibrium

Received: 24 June 2002 / Accepted: 16 September 2002 / Published online: 12 December 2002
© Springer-Verlag 2002

Abstract The climate of the last glacial maximum (LGM) is simulated with a coupled climate model. The simulated climate undergoes a rapid adjustment during the first several decades after imposition of LGM boundary conditions, as described in Part 1, and then evolves toward equilibrium over 900 model years. The climate simulated by the coupled model at this period is compared with observationally-based LGM reconstructions and with LGM results obtained with an atmosphere-mixed layer (slab) ocean version of the model in order to investigate the role of ocean dynamics in the LGM climate. Global mean surface air temperature and sea surface temperature (SST) decrease by about 10 °C and 5.6 °C in the coupled model which includes ocean dynamics, compared to decreases of 6.3 and 3.8 °C in slab ocean case. The coupled model simulates a cooling of about 6.5 °C over the tropics, which is larger than that of the CLIMAP reconstruction (1.7 °C) and larger than that of the slab ocean simulation (3.3 °C), but which is in reasonable agreement with some recent proxy estimates. The ocean dynamics of the coupled model captures features found in the CLIMAP reconstructions such as a relative maximum of ocean cooling over the tropical Pacific associated with a mean La Niña-like response and lead to a more realistic SST pattern than in the slab model case. The reduction in global mean precipitation simulated in the coupled model is larger (15%) than that simulated with the slab ocean model (~10%) in conjunction with the enhanced cooling. Some regions, such as the USA and the Mediterranean region, experience increased precipitation in accord with proxy

paleoclimate evidence. The overall much drier climate over the ocean leads to higher sea surface salinity (SSS) in most ocean basins except for the North Atlantic where SSS is considerably lower due to an increase in the supply of fresh water from the Mississippi and Amazon rivers and presumably a decrease in salt transport by the weakened North Atlantic overturning circulation. The North Atlantic overturning stream function weakens to less than half of the control run value. The overturning is limited to a shallower depth (less than 1000 m) and its outflow is confined to the Northern Hemisphere. In the Southern Ocean, convection is much stronger than in the control run leading to a stronger overturning stream function associated with enhanced Antarctic Bottom Water formation. As a result, Southern Ocean water masses fill the entire deep ocean. The Antarctic Circumpolar Current (ACC) transport through the Drake Passage increases by about 25%. The ACC transport, despite weaker zonal winds, is enhanced due to changes in bottom pressure torque. The weakening of the overturning circulation in the North Atlantic and the accompanying 30% decrease in the poleward ocean heat transport contrasts with the strengthening of the overturning circulation in the Southern Ocean and a 40% increase in heat transport. As a result, sea ice coverage and thickness are affected in opposite senses in the two hemispheres. The LGM climate simulated by the coupled model is in reasonable agreement with paleoclimate proxy evidence. The dynamical response of the ocean in the coupled model plays an important role in determining the simulated, and undoubtedly, the actual, LGM climate.

S.-J. Kim (✉)
Division of Earth and Ocean Sciences,
Duke University, Durham, NC 27708, USA
E-mail: sjkim@duke.edu

G.M. Flato · G.J. Boer
Canadian Centre for Climate Modelling and Analysis,
Meteorological Service of Canada,
University of Victoria, PO Box 1700,
Victoria, BC V8W 2Y2, Canada

1 Introduction

The Earth's climate has fluctuated between glacial and interglacial states and the most recent epoch, the "Last Glacial Maximum" or LGM peaked about 21,000 years

ago. Geological and geochemical proxy data have been used to provide a broad picture of the LGM climate (e.g., CLIMAP 1976, 1981), but these data are limited in their ability to reveal the manner in which the climate system operated. As an adjunct to the study of proxy data, physically based climate simulation models have been used to study the mechanisms associated with such a marked climate change.

Several kinds of numerical models have been applied to study the LGM climate. Atmosphere-only models for which LGM sea surface temperature (SST) and ice cover based on paleoclimate reconstructions are specified have had some success in simulating the change in atmospheric circulation, hydrological budget, and other climate processes over land (Gates 1976; Manabe and Hahn 1977; Kutzbach and Guetter 1986, etc.). However, the simulated climate is inevitably constrained by the specified SST which has substantial uncertainty. For example, tropical cooling of less than 2 °C in the CLIMAP reconstruction is contradicted by recent lines of proxy evidence which suggest cooling of more than 5 °C in the tropical regions (Rind and Peteet 1985; Guilderson et al. 1994; Thompson et al. 1995, etc.).

Other simulations have employed a constant depth mixed layer or “slab” ocean model coupled to an atmospheric general circulation model (Manabe and Broccoli 1985; Broccoli 2000; Vettoretti et al. 2000; Joussaume and Taylor 2000). In these models the SST is determined through the thermodynamic balance of the mixed layer in the presence of a specified heat flux convergence term, which is intended to represent the current heat transport process. In such models, this specified oceanic heat transport does not change in response to perturbed forcing conditions. Paleoclimate data suggest, for instance, that the LGM ocean exhibited a much weaker and shallower glacial North Atlantic overturning circulation (Duplessy et al. 1988; Boyle and Keigwin 1987) so that changes in ocean dynamics are expected to be of importance.

Another approach uses ocean-only models to investigate the change in ocean circulation and its impact on the LGM climate (e.g. Fichefet et al. 1994), but the ocean-only models require the specification of uncertain LGM ocean boundary conditions while neglecting atmospheric feedbacks. Coupled models of intermediate complexity simplifying either atmosphere (Weaver et al. 1998), ocean, or both (e.g., Ganopolski et al. 1998), attempt to include some of the atmosphere–ocean feedbacks. However, the simplified representation of atmosphere behavior strongly constrains the atmospheric response to LGM forcing and the magnitude of atmosphere–ocean feedbacks associated with the large climate perturbation that is the LGM.

Fully coupled models (i.e., models that include three-dimensional representations of atmospheric and oceanic general circulation) are the most comprehensive and physically based tool currently available for simulating the climate of the LGM. To date few such simulations have been performed and the results vary considerably.

Bush and Philander (1999) integrate the GFDL coupled model for only 15 years after imposing LGM CO₂, glacial ice sheets, reduced sea level, and LGM orbital parameters. The simulation exhibits a cooling of 5 to 6 °C over the tropical Pacific, a slight warming of the Southern Ocean, and a decrease in Antarctic sea-ice extent. The simulated tropical temperatures agree reasonably well with recent proxy estimates, but there is disagreement at high latitudes. This difference is most likely a consequence of the short integration time as described in Kim et al. (2002) (hereafter referred to as KFBM). The tropical SST is largely governed by the atmosphere and upper ocean dynamics which have short response times at low latitudes. In high latitudes, however, the model is still far from equilibrium due to the longer time scales associated with deep ocean feedbacks.

In a more recent LGM simulation, Hewitt et al. (2001) integrate the Hadley Centre coupled model for 770 years. They find a tropical cooling of less than 2 °C and anomalously warm temperatures over parts of the North Atlantic which they attribute to increased northward heat transport by a stronger North Atlantic overturning circulation. After 270 years of integration using the MRI coupled model under LGM conditions, Kitoh et al. (2001) obtain a 1.7 °C cooling over the tropics with warming patches in the eastern Pacific and increased North Atlantic overturning. Although these later results are tending toward their LGM equilibrium, disagreements with paleoclimate reconstructions remain.

A coupled atmosphere–ocean–sea ice–land surface climate system model is used to investigate the response to the imposition of glacial boundary conditions. The rapid initial adjustment process during the first century is described in KFBM. The integration reported here comprises some 900 years of periodically synchronous coupled simulation. Although some quantities continue to adjust even at this time, overall features should be representative of the LGM climate. We attempt some comparisons with paleoclimate data but accept that the proxy estimates are not robust. The main interest in the study is to investigate how the climate system operates under glacial conditions. The role of ocean dynamic feedbacks in determining the LGM climate is investigated through a comparison to the LGM climate obtained from the atmosphere–mixed layer ocean version of the model.

2 Model and coupling

The model employed in the current study is the second generation Canadian Centre for Climate Modelling and Analysis (CCCma) coupled general circulation model (CGCM2). A detailed description of the atmosphere, ocean, sea ice, and land surface components of CGCM2 is given in other papers (McFarlane et al. 1992; Flato et al. 2000; Flato and Boer 2001; KFBM and references therein). Only a brief summary is provided here.

The atmospheric component of CGCM2 is a primitive equation model characterized by T32 horizontal resolution corresponding to a 3.75° Gaussian grid, and 10 vertical levels. Cloud formation and moist convective processes are parametrized through relative

humidity and by a convective adjustment scheme. The effects of clouds, water vapor, carbon dioxide, oxygen, and ozone are included in the calculation of solar and terrestrial radiation. The surface energy balance is evaluated using the force-restore method and soil moisture is represented in terms of a simple variable depth bucket model. The surface albedo is evaluated depending on the surface type. A simple river routing scheme is included to represent the freshwater flux into the ocean. The scheme involves instantaneous transfer of runoff from land to the ocean using specified river drainage basins which have been modified to reflect the altered land distribution and ice sheet topography of the LGM.

The oceanic component is a modified version of the GFDL MOM version 1.1 (Pacanowski et al. 1993). The horizontal grid spacing is $1.875^\circ \times 1.875^\circ$ with 29 vertical layers. The ocean model includes realistic bottom topography and ocean mixing is represented by vertical and isopycnal diffusion, along with the eddy stirring parameterization of Gent and McWilliams (1990) (GM). When the density stratification is unstable, convective adjustment is performed by increasing the vertical diffusivity. CGCM2 includes a dynamic–thermodynamic sea-ice model. Sea-ice dynamics is represented using the cavitating fluid rheology of Flato and Hibler (1992), while sea-ice thermodynamics is represented by a slightly modified version of the 0-layer scheme of Semtner (1976).

The atmosphere and ocean components interact once per day exchanging heat, fresh water, and momentum. The coupling procedure of this model is basically the same as that of CGCM1 (Flato et al. 2000) except that the ice dynamics component is included. Monthly heat and freshwater flux adjustment fields are applied for all coupled model experiments, but have an RMS magnitude of about half that of CGCM1.

3 Experiments

The results of three experiments are studied. The control simulation has a specified CO_2 concentration of 330 ppm, and a contemporary land mask and topography. This experiment is referred to as “CTRL”. The other two experiments employ LGM boundary conditions. The simulation employing a full 3-D ocean representation is termed the “LGMC” simulation (C indicates a fully coupled ocean). It features a decreased CO_2 concentration of 235 ppm, a value chosen to reproduce the greenhouse gas forcing difference between contemporary and LGM conditions (Barnola et al. 1987), a modified land mask based on sea level lowering by 120 m (Fairbanks 1989), and ice-sheet topography using the ICE-4G reconstruction of Peltier (1994). The mass balance of the ice sheet is not a prognostic variable. Orbital parameters and vegetation and soil types are unchanged. Although the effect of vegetation on the LGM climate may not be negligible on a regional basis, the global impact is of less importance (Crowley and Baum 1997; Wypytta and McAvaney 2001). A more detailed description of the LGM boundary conditions is found in KFBM.

The simulation employing the mixed layer ocean is referred to as the LGMM simulation (M means mixed layer ocean). It has almost identical boundary conditions to the LGMC simulation. The LGMM simulation was performed by Vettoretti et al. (2000) and is a contribution to the PMIP intercomparison project (Joussaume and Taylor 2000). We compare LGMC and LGMM results to highlight the importance of ocean dynamics in LGM climate.

4 Accelerated coupled simulation

A fully coupled GCM is computationally intensive even using a state-of-the-art super computer. The atmospheric component generally consumes the largest share of the computing effort but it equilibrates rather quickly to the ocean surface state. Conversely, the ocean component takes relatively less computing effort but it

responds much more slowly. A significant amount of computational time can be saved, by accelerating the oceanic component during the simulation.

An asynchronous coupling method was first introduced by Manabe and Bryan (1969). In this method, the atmosphere and the ocean sub-models are integrated with different time steps. While the method is successful with annual mean forcing (Manabe and Stouffer 1988), it is not suitable when the annual cycle is included (Harvey 1986; Sausen and Voss 1996). As an alternative, a periodically synchronous coupling method was proposed by Gates (see Schlesinger 1979). More recently, the periodically synchronous coupling method has been tested with a simple atmosphere–ocean model (Harvey 1986; Sausen and Voss 1996; Voss and Sausen 1996) and with the ECHAM/LSG coupled GCM (Voss et al. 1998). The periodically synchronous coupling method has been successful in representing the annual cycle and a version of it has been adopted here.

The scheme is essentially that described by Voss and Sausen (1996) and consists of period of a coupled simulation, followed by a period of ocean-only integration and so on. During the period of coupled integration the atmosphere and ocean communicate fully. The fluxes of energy, fresh water, and momentum generated during this period are stored. Symbolically $f_c(t)$ represents the averaged annual cycle of the forcing obtained during the period of coupled integration. After the period of coupled integration, the ocean component is integrated with annual cycle forcing specified as

$$f_o(t) = \hat{f}_o + (f_c(t) - \bar{f}_c), \quad (1)$$

where \bar{f}_c is the annual mean of $f_c(t)$, while \hat{f}_o represents the weighted annual mean ocean forcing which includes some memory of the previous forcing period. The memory term in the ocean forcing acts to damp possible overshoots of the climate during the ocean only period.

The memory term is computed as

$$\hat{f}_o = \frac{g\hat{f}_{o(old)} + \bar{f}_c}{g + 1}, \quad (2)$$

where $\hat{f}_{o(old)}$ is the weighted annual mean of the ‘last’ ocean only period and g represents the weight. In the current study $g = 2$ as in previous work (Voss and Sausen 1996; Voss et al. 1998). A more detailed description of the method for evaluating the memory term and the ocean forcing term is found in Voss and Sausen (1996).

The abrupt imposition of a forcing change at the beginning of a simulation leads to a rapid system adjustment and the potential for overshooting is large (e.g., Sausen and Voss 1996). We therefore integrate the system in a fully coupled mode for the first 100 years and then use ocean acceleration for the remainder of the simulation. The memory term \hat{f}_o is especially important for the ‘first’ ocean only integration in minimizing the systematic error. We use the last 30 years of fluxes

retained from the initial synchronous period. The overshooting is also sensitive to the time span of the ocean only integration. In the current study, we set the period of fully coupled integration to 1 year and the period of ocean-only integration to 5 years. This proportion has been used previously in a simple coupled GCM study (Harvey 1986).

5 Simulated LGM climate

The first 80 years of transient climate response to the imposed glacial boundary conditions are described in the companion paper (KFBM). The temporal evolution of globally averaged annual-mean quantities for the LGMC (dashed) and the CTRL simulation (solid) is shown in Fig. 1. The vertical line in Fig. 1 indicates the time when ocean acceleration is initiated for the LGMC simulation (no ocean acceleration is applied to the control simulation). After rapid adjustment during the first several decades the system slowly evolves towards the LGM state and after 900 years it is markedly different from either the transient state or the control climate.

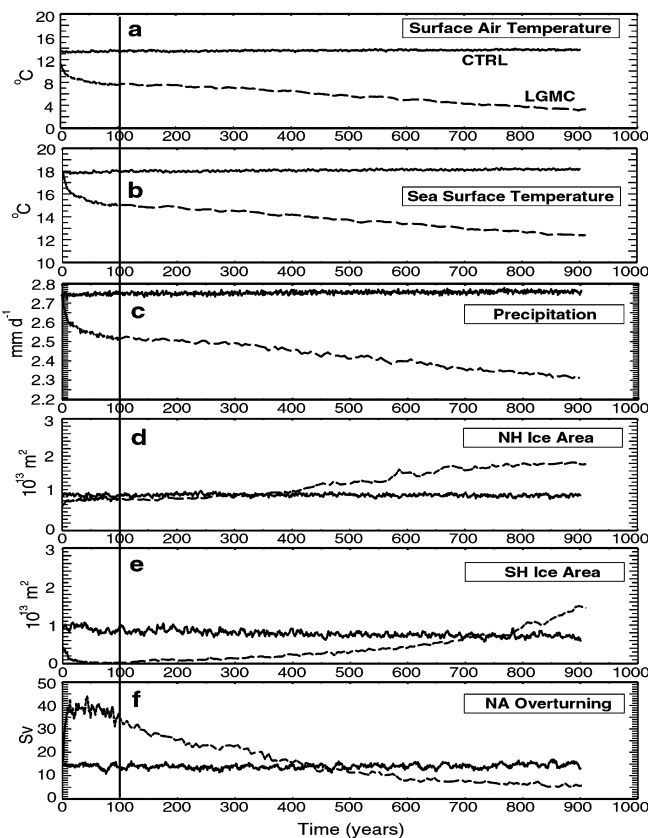


Fig. 1 Time series of annual-mean, **a** surface air temperature, **b** sea surface temperature, **c** precipitation, **d** NH ice area, **e** SH ice area, and **f** maximum North Atlantic overturning stream function. The vertical line separates the synchronous and asynchronous portions of the LGM integration

Surface air temperature (SAT) and SST decrease with time and after 900 years SAT has decreased by 10.1 °C and SST by 5.6 °C on the global average. Precipitation decreases to about 2.34 mm/day at this time, which is a 15% reduction from the control value. In the Northern Hemisphere (NH), the annual-mean sea ice area increases gradually up to $1.8 \times 10^{13} \text{ m}^2$ from about $0.96 \times 10^{13} \text{ m}^2$, whereas in the Southern Hemisphere (SH) it decreases initially to near zero but slowly recovers with time eventually reaching and exceeding the control value by the end of the simulation. The near absence of the SH sea ice during the early part of the simulation is due to a stronger oceanic heat flux driven by enhanced convection. The mismatch of global-mean values between the two experiments at the initial time is due to the modification of the land mask as described in KFBM. The transient increase in ocean convection in the North Atlantic also leads to a marked initial increase of the North Atlantic overturning stream function (see KFBM). As the ocean convection slowly weakens with time, the North Atlantic overturning circulation gradually decreases and after 900 years it is about half the control value.

Results averaged over the last 50 years of the simulation are analyzed and compared to the reconstructed LGM climate obtained from proxy data and to the results obtained from a slab ocean version of the model. Of course, the slab ocean model equilibrates much more quickly (within 50 years) than the coupled model (Vettoretti et al. 2000). The last 10 years of the slab ocean model results are averaged for comparison. We focus primarily on the surface quantities since most of the paleoclimate observations are representative of the surface climate. The CGCM2 control climate is briefly described in KFBM.

5.1 Temperature

5.1.1 Surface air temperature

The geographic distribution of the annual mean SAT change between the LGMC and the CTRL experiment is displayed in Fig. 2a. The largest SAT decrease, more than 30 °C, is found over the Laurentide and Fennoscandian ice sheet due to the change in elevation and the higher surface albedo. The strong land/sea contrast and the cold tongue over the equatorial Pacific, a La Niña-like feature, is manifest early in the transient adjustment and persists as equilibrium is approached. By contrast, the initial strong warming seen in the Southern Ocean and the northern North Atlantic (KFBM) disappears after 900 years primarily due to the reduction of upward ocean heat flux associated with the weakening of ocean convection in the North Atlantic and deep-ocean cooling in the Southern Ocean as described later.

The geographic distribution of SAT change obtained from the LGMM simulation is shown in Fig. 2b and its difference from the LGMC simulation in Fig. 2c. The

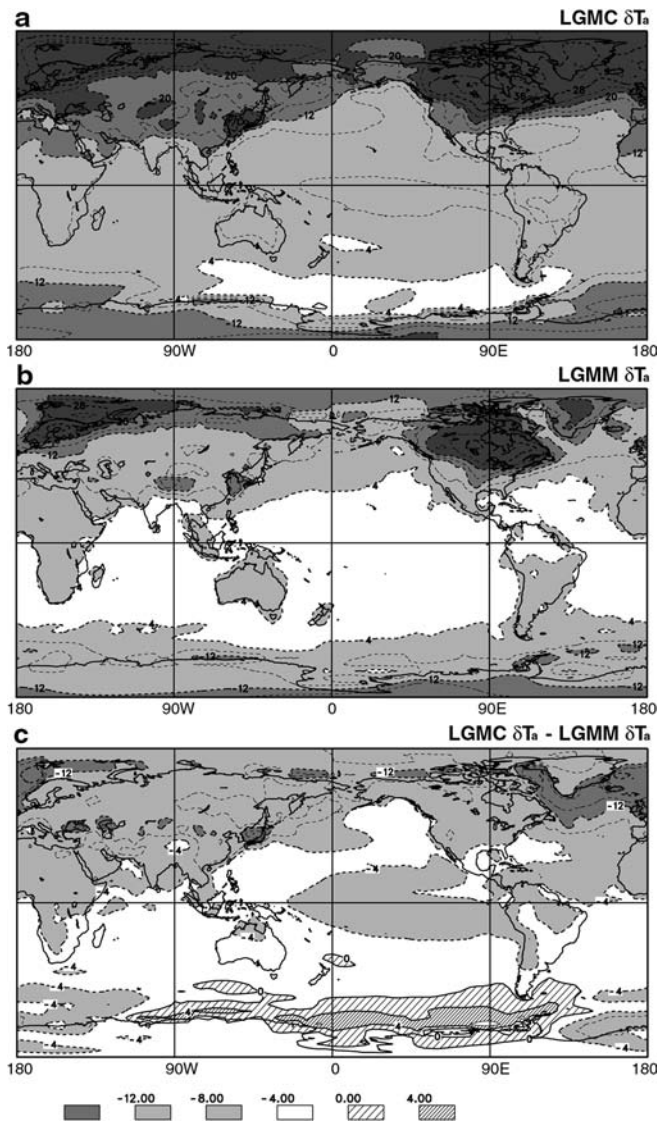


Fig. 2 Geographic distribution of the change (LGM minus control) in annual-mean surface air temperature simulated in the, **a** coupled model, **b** slab ocean model, and **c** difference of the change in SAT between the two model versions. Contour interval is 4 °C

strong cooling over the ice sheets and the land/sea contrast of surface temperature are the common feature in both model versions, but some revealing differences are apparent. The LGMC temperature simulation exhibits more structure over the oceans including a La Niña-like response in the tropical Pacific. The same mechanisms responsible for the El Niño-like response under warming conditions (Yu and Boer 2002) operate in the opposite sense to produce the La Niña-like response in a colder climate. Cooling over the northern North Atlantic is greater in the LGMC simulation, but weaker over the Pacific sector of the Southern Ocean. In the northern North Atlantic, sea ice extends farther south in LGMC than in LGMM, while in the Pacific sector of the Southern Ocean sea-ice is less extensive in the LGMC simulation. The hemispheric difference in sea-ice distribution in the LGMC simulation is

associated with the change in ocean meridional heat transport described later. Overall, cooling is larger in the LGMC simulation than in the LGMM simulation especially over land (Fig. 2c). Since the difference between the two simulations is in the representation of the ocean, the SAT and other differences are necessarily and ultimately result of coupled and ocean feedback processes which operate in the coupled but not the slab ocean model as is discussed subsequently.

Globally averaged annual mean SAT change (−10.1 °C) is larger in the coupled model than in the slab ocean model (−6.3 °C). This is consistent with other results indicating a larger temperature response in a coupled model compared to that of a slab ocean model. Using the CCCma atmosphere model coupled to a mixed layer ocean model, Boer et al. (1992) obtain a global mean warming of 3.5 °C for a doubling of CO₂ concentration, while Boer and Yu (2002) report a warming of about 4.0 °C in a stabilization simulation using a fully coupled model for forcing approximately that of CO₂ doubling (see Boer et al. 2000 for experimental design). Similarly, a simulation using the GFDL atmospheric model and a mixed layer ocean gives a global mean temperature increase of 3.9 °C for a doubling of CO₂ (Manabe et al. 1991), while a simulation using the GFDL coupled model gives an increase of 4.5 °C (Stouffer and Manabe 1999).

There is also some evidence that model sensitivity tends to be larger in colder than in warmer climates, presumably due to stronger snow and sea-ice feedbacks. For example, Manabe et al. (1991) obtain a global mean cooling of 6.2 °C and warming of 4.0 °C for halving and doubling of atmospheric CO₂, while Hansen et al. (1997) find a cooling of 4.7 °C and warming of 3.2 °C with a 2% decrease and increase in solar irradiance. For these models, climate sensitivity is apparently about 50% larger for negative compared to positive radiation forcing changes.

The boundary conditions used in the LGM simulations incorporate reduced CO₂ to about two thirds of its present value and ice sheet topography, with the associated decrease in surface temperature with height and increased albedo. In comparison to the LGMM simulation, the overall cooling in the LGMC simulation is larger indicating the increased sensitivity of a model which now includes coupled and ocean feedback processes together with the increased sensitivity exhibited in colder climates.

5.1.2 Surface ocean temperature

Figure 3 compares the August SST change for the LGMC and LGMM simulations with the reconstructed August SST changes from CLIMAP (1976) and CLIMAP (1981). The temperature reconstruction in Fig. 3c is a digitization of the diagram in CLIMAP (1976) while Fig. 3d is obtained from the IRI/LDEO climate data library (<http://iridl.ldeo.columbia.edu>).

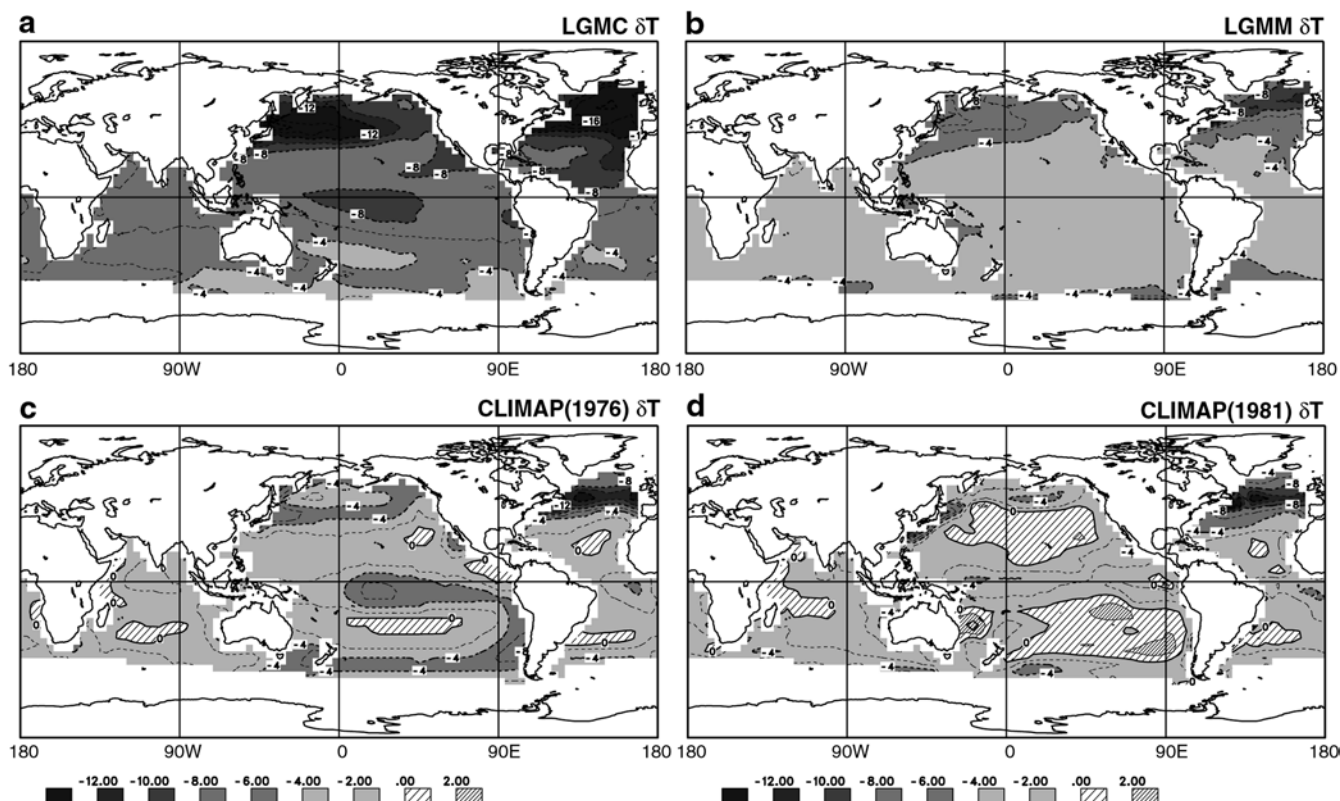


Fig. 3 Geographic distribution of the change in August sea surface temperature simulated in the, **a** coupled model, **b** slab ocean model; reconstructed by **c** CLIMAP (1976), and **d** CLIMAP (1981). Contour interval is 2 °C

Table 1 Lists of observed and simulated tropical (25°S–25°N) LGM surface temperature change from literature. Bold face indicates proxy estimates

Degree of cooling	Methods/models	References
	Planktonic assemblages	CLIMAP (1976; 1981); Barrows et al. (2000)
Modest cooling	Foraminifer $\delta^{18}\text{O}$	Broecker (1986)
	Alkenone	Sikes and Keigwin (1994); Bard et al. (1997)
$-2.5\text{ °C} < \Delta T$	AGCM + mixed layer ocean	Broccoli (2000)
	EMBM + OGCM	Weaver et al. (1998)
	UKMO coupled model	Hewitt et al. (2001)
	MRI coupled model	Kitoh et al. (2001)
	Ice core $\delta^{18}\text{O}$	Pierrehumbert (1999)
Moderate cooling	Mg/Ca ratio	Elderfield and Ganssen (2000)
	Simple AGCM + Zonal Mean OGCM	Ganopolski et al. (1998)
$-5\text{ °C} < \Delta T < -2.5\text{ °C}$	AGCM + mixed layer ocean	PMIP (Joussaume and Taylor 2000)
Strong cooling	Snow line depression	Rind and Peteet (1985)
	(Sr/Ca) Coral	Guilderson et al. (1994); Beck et al. (1997); McCulloch et al. (1999)
$\Delta T < -5\text{ °C}$	Tropical ice core $\delta^{18}\text{O}$	Thompson et al. (1995)
	Pollen	Colinvaux et al. (1996)
	Reassessed planktonic assemblage	Mix et al. (1999)
	Groundwater noble gas	Stute et al. (1995); Weyhenmeyer et al. (2000); Aeschbach-Hertig et al. (2000)
	GFDL coupled model	Bush and Philander (1999)

The degree of cooling obtained in the LGMCM run is relatively high in the North Atlantic, northwestern Pacific, and equatorial Pacific, as in CLIMAP, especially with the CLIMAP (1976) reconstruction, but a large discrepancy is seen over the subtropics. In the

reconstructions, the warming patches in the subtropics lead to overall tropical cooling of less than 2 °C in the 1976 version and less than 1 °C in the 1981 version. This is an area of considerable debate as summarized in Table 1 which compares the tropical temperature

change from a range of paleoclimate proxy estimates and model studies. The degree of tropical temperature depression tends to depend on the type of geological evidence used for its estimation. For example, inferences based on foraminifer $\delta^{18}\text{O}$ and recent alkenone analysis suggests a modest tropical cooling, consistent with or slightly colder than the CLIMAP reconstruction based on planktonic assemblages. On the other hand, other proxy estimates from various sources, such as snow line depression, coral, tropical ice core, noble gases from ground water, pollen, etc., suggest tropical cooling of more than 5 °C in agreement with our coupled model simulation.

Other coupled models simulate various degrees of tropical cooling. For example, the UKMO and MRI coupled models produce tropical cooling of less than 2 °C, whereas Bush and Philander (1999) using a version of the GFDL coupled model simulate a larger tropical cooling of 5 ~ 6 °C despite a rather short 15 year simulation.

The geographic pattern of the SST change in the LGMC simulation appears to better resemble the temperature pattern of the CLIMAP reconstruction than does that of the LGMM simulation. The LGMC simulation clearly exhibits features associated with ocean dynamics, found also in CLIMAP, but absent in the LGMM results. These include the relatively cold tongue in the equatorial Pacific and Atlantic, cold patches associated with coastal upwelling in the southeastern Pacific, off the southeastern tips of Africa, Australia, and South America, and the comparative warmth of the subtropical ocean gyres. The agreement between the coupled model and CLIMAP SST patterns, especially compared to the LGMM result, indicates the important role of ocean dynamics in shaping the LGM climate response as is described in more detail in following section.

Results are compared more quantitatively in terms of second moment statistics in the BLT diagram (Boer and Lambert 2001) of Fig. 4 taking the CLIMAP reconstructions as reference values. The ratio of spatial variances is indicated by the dashed lines and the closeness of the point to the bold dashed line indicates its closeness to a perfect ratio of 100%. The distance between a point and the “star” in the bottom left corner of the diagram measures its mean square difference while the rays emitting from the right hand corner of the diagram indicate correlation.

As expected from the pattern of SST change in Fig. 3, the smooth LGMM pattern has a much lower spatial variance (solid triangles and crosses) than does CLIMAP, with values less than 30% of the CLIMAP variance. The LGMC simulation (solid and open circles) exhibits spatial variances that are overall more comparable to those of CLIMAP. Spatial correlation between the LGMC simulation and CLIMAP is reasonably high (> 50%) in the NH, whereas it is lower in the SH presumably due to less cooling in the LGMC

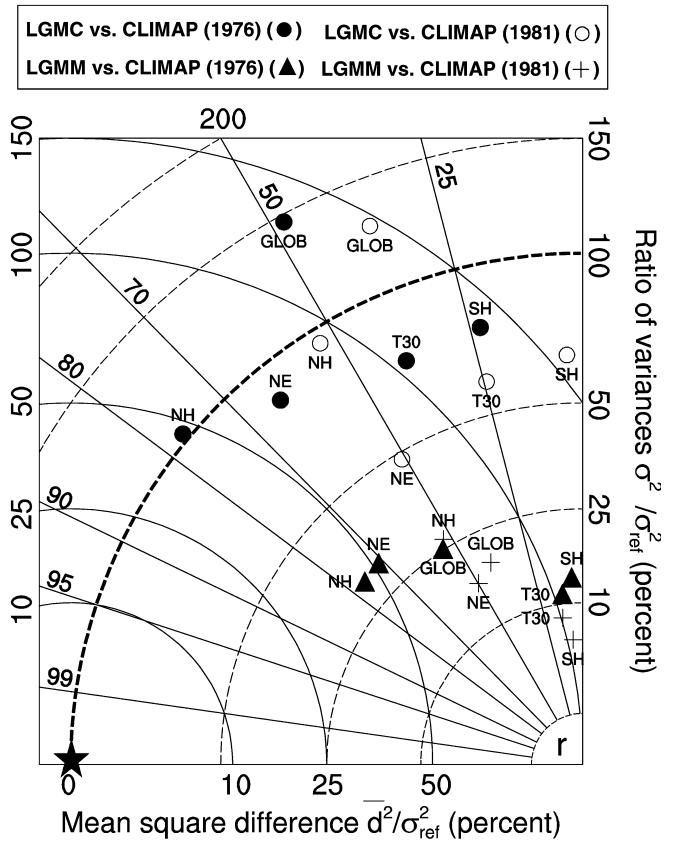


Fig. 4 The BLT diagram illustrating mean square differences, variances, and correlations between models and observations. *Solid and open circles* indicate results for the coupled model versus CLIMAP (1976) and CLIMAP (1981) and *triangles and crosses* for the slab ocean model versus CLIMAP (1976) and CLIMAP (1981). Statistics for global domain are represented as *GLOB*, Northern Hemisphere as *NH*, Southern Hemisphere as *SH*, Northern Hemisphere extratropics as *NE*, and tropics between 30°S–30°N as *T30*. Units percent

simulation relative to CLIMAP at the northern margin of the Antarctic sea ice in the Pacific sector. In the NH, the LGMM simulation exhibits also a relatively high correlation with CLIMAP, even though the variance is low. Spatial correlation between the LGMC simulation and CLIMAP (1976) is everywhere higher than that with CLIMAP (1981).

To summarize, the global and tropical mean SST changes in the LGMC simulation are –5.6 °C and –6.5 °C, respectively, which are larger than CLIMAP (1976) (–2.5 and –1.7 °C), CLIMAP (1981) (–1.3 and –1.0 °C), or the LGMM simulation (–3.8 and –3.3 °C). However, the larger tropical cooling in the LGMC simulation is in better agreement with recent proxy evidence, the balance of which suggests tropical cooling less than 5 °C (Table 1). More particularly, the ocean dynamics in the coupled model produces stronger and more realistic SST structures in the simulated LGM climate as measured by the spatial variances and correlation.

5.1.3 Zonal-mean temperature

Zonally averaged temperature changes in the atmosphere and ocean are plotted in Fig. 5. In the atmosphere, the largest cooling is found at and near the surface in the northern high latitudes associated with the strong cooling over the ice sheet. At tropical and SH latitudes the cooling is weaker, resulting in a strong interhemispheric asymmetry in the near surface temperature change. The relative maximum cooling in the tropical upper troposphere mirrors the relative maximum warming in global warming integrations with the model (Boer et al. 2000) as expected from changes in the convective mixing processes. The increase in the tropical lapse rate in the LGMC experiment is consistent with the descent of the snow line and vegetation zones which occurred throughout the tropics during the LGM (Webster and Streten 1978; Rind and Peteet 1985). This increase in lapse rate is also consistent with the comparatively large surface cooling noted in the previous section.

In the ocean, the largest cooling is located at northern mid-latitudes, mainly due to the change in the North Atlantic overturning circulation and the associated northward heat transport as described later. A relatively smaller cooling is found in water masses of Southern Ocean origin, i.e., the water mass at the mid-depths of the SH and the water mass at the bottom close to

Antarctica which is associated with Antarctic bottom water (AABW). Overall, the deep ocean exhibits a temperature reduction of slightly more than 4 °C in the coupled model simulation. This amount of cooling is made possible in part by a warm bias (of roughly 1 °C) in the control deep water.

Variations in marine oxygen isotope ratio ($\delta^{18}\text{O}$) result in part from changes in ice volume and in part from changes in ocean temperature. Glacial-interglacial $\delta^{18}\text{O}$ variations recorded in shells of benthic foraminifera have been used as a proxy for deep ocean temperature change after excluding the contribution from the change in the ice volume. The generally accepted glacial-interglacial $\delta^{18}\text{O}$ change is near 1.7 per mil, of which about 1.25 per mil has been suggested to be due to the change in ice volume (Fairbanks 1989; Guilderson et al. 1994). The remaining 0.45 per mil is thought to be due to the change in deep ocean temperature. The 0.45 $\delta^{18}\text{O}$ change corresponds to about 2 °C cooling based on 0.22 per mil $\delta^{18}\text{O}/1\text{ °C}$ temperature. According to this the magnitude of the simulated deep ocean cooling is overestimated. Recently, however, Schrag et al. (1996) using pore fluids from deep sea sediments in the Atlantic suggest that the $\delta^{18}\text{O}$ change due to ice volume may be closer to 0.8 per mil implying a deep Atlantic ocean cooling of about 4 °C, a value close to the model result.

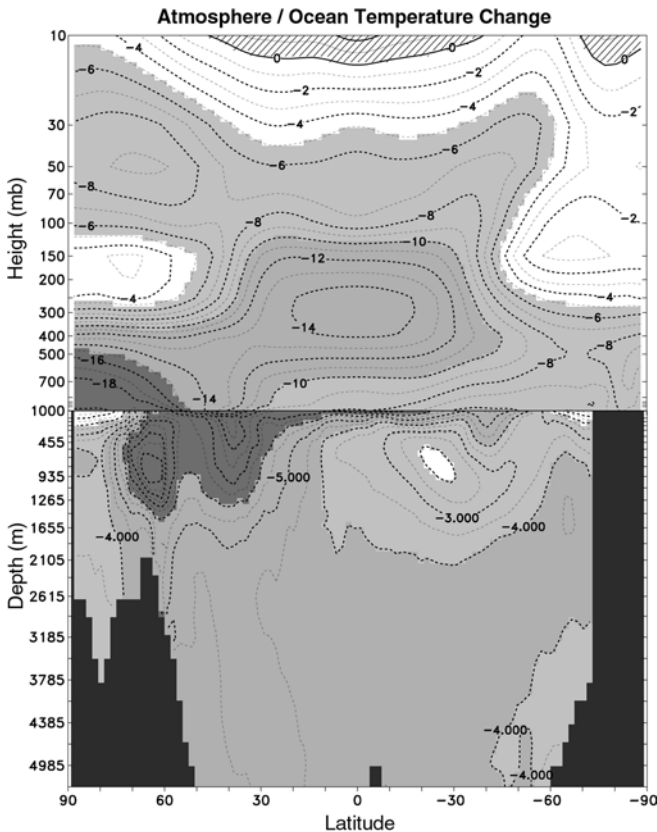


Fig. 5 Zonally averaged annual-mean atmosphere and ocean temperature change. Contour intervals are 1 °C for the atmosphere and 0.5 °C for the ocean

5.2 Surface heat balance

Changes in surface temperature are governed by, and influence, changes in surface heat fluxes. We investigate how the surface heat flux has changed under LGM conditions and how LGMC results differ from LGMM results.

The energy budget of the upper 50 m layer of the ocean is written as (Boer 1993)

$$C_* \frac{\partial T}{\partial t} = (S + F) + (LE + H) + A = R + B + A \quad (3)$$

where C_* is the heat capacity of the layer, T the temperature, S the shortwave and F the longwave radiative heat fluxes, LE the latent and H the sensible heat fluxes across the surface. Here A represents the effect of vertical and horizontal heat transport in the layer. $R = S + F$ is the net radiative heat fluxes and $B = LE + H$ is the net turbulent heat fluxes. In quasi-equilibrium, the rate of change term is small and the difference in heat budget terms between LGM equilibrium and control climates is $\delta R + \delta B + \delta A = 0$. Note that the sign convention is that all fluxes are positive if they act to warm and negative if they act to cool the layer.

5.2.1 Radiative and turbulent heat fluxes

Figure 6a displays the geographic distribution of the change in the net radiative heat flux δR simulated in the coupled model. Over North America and Europe,

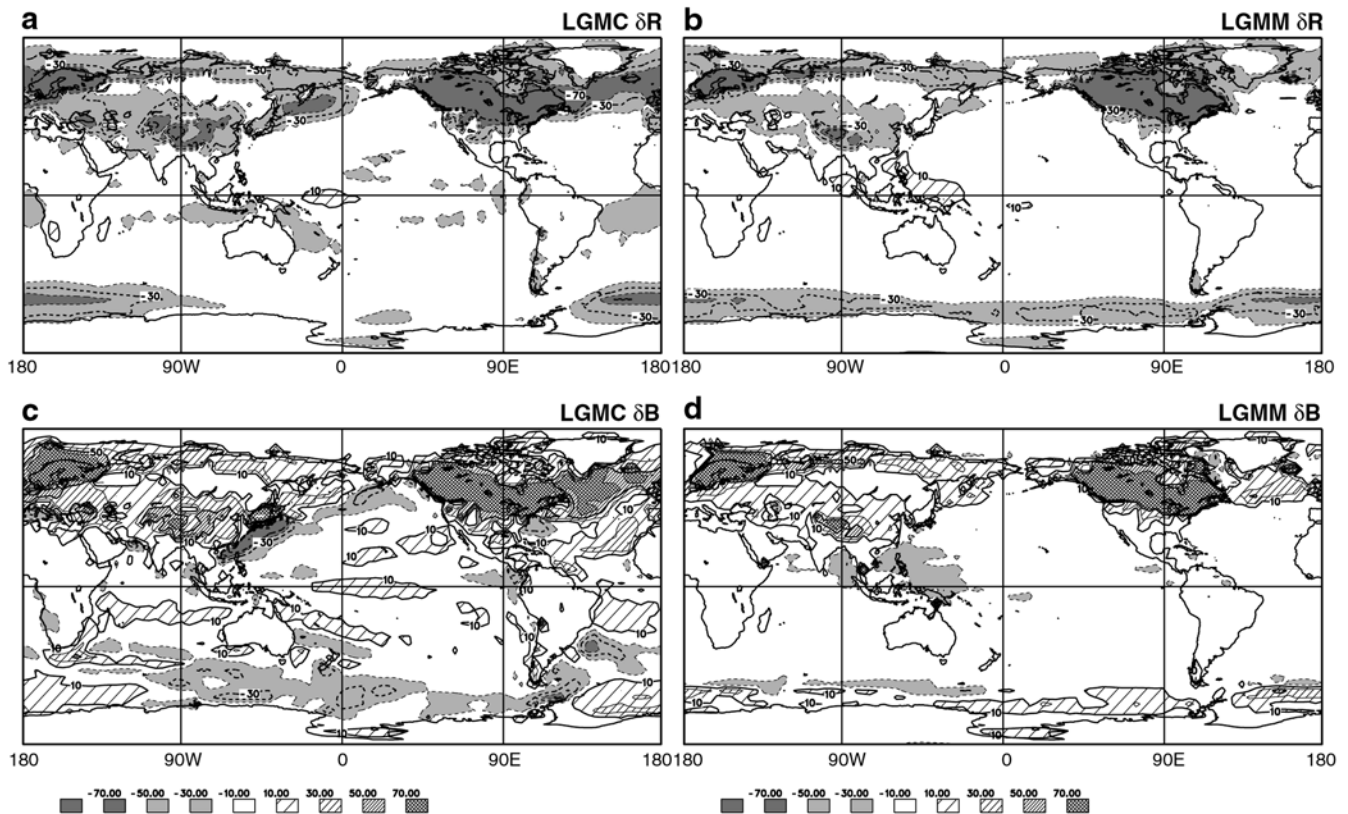


Fig. 6 Geographic distribution of the change in annual-mean net radiative heat fluxes simulated in the, **a** coupled model, **b** slab ocean model; net turbulent heat fluxes in the, **c** coupled model, and **d** slab ocean model. Contour interval is 20 W m^{-2}

the northern North Atlantic, and some portions of the Southern Ocean, the radiative flux change is such as to cool the surface due to increased surface albedo over ice sheets and increased sea ice cover. There is comparatively little change in radiative heat flux over the ocean. Figure 6b shows the change in the net radiative heat flux in the slab ocean model simulation. The changes in δR are broadly similar in the two simulations although there are differences in the net radiative heat flux change over the northern North Atlantic, the northwest Pacific, and the Pacific sector of the Southern Ocean, largely due to differences in sea-ice cover. A slight discrepancy is also found over the western Pacific where the change in radiative heat flux in the LGMC simulation is larger than that of LGMM simulation. This difference is presumably associated with the La Niña-like response.

Figure 6c and d shows the geographic distribution of the change in the net turbulent heat fluxes δB in the two simulations. Over most areas, especially in North America and northern Europe, the change in turbulent (mainly latent) heating is such as to warm the surface, reflecting a reduction in evaporation and sensible heat flux associated with the reduction in surface temperature. The primary differences in turbulent heat flux between the LGMC and LGMM simulations occur in regions strongly affected by ocean transport changes such as the equatorial upwelling and western boundary

current regions. Differences in δB are also found where sea-ice cover differs between the two simulations such as over the northern North Atlantic and over the Southern Ocean. Since the coupled model cools more than the slab ocean model (Fig. 2), the change in turbulent heat flux is generally larger.

Overall, the ocean dynamics of the coupled model produces substantial differences in the net, especially turbulent, heat fluxes compared to that of the slab ocean model through a modification of SST patterns and the sea-ice cover.

5.2.2 Oceanic advective heat flux and its impact on SST

Over land, where $\delta A = 0$, equilibrium energy balance requires that $\delta R + \delta B = 0$ (a small term associated with snow melt is neglected here), the change in radiative heating is balanced by the change in turbulent heat flux. Over the ocean, however, changes in ocean heat transport are important in the new energy balance and therefore influence the SST change. The change in SST due to the change in the ocean transport is estimated by assuming equilibrium and rewriting (3) as $S + F^\downarrow - \sigma T^4 + B + A = 0$ for $F = F^\downarrow - \sigma T^4$, where F^\downarrow is the incident and $-\sigma T^4$ the emitted longwave at the surface. Taking differentials and rearranging gives

$$\delta T = \frac{\delta A + (\delta S + \delta F^1)}{4\sigma T^3 - \delta B/\delta T} \quad (4)$$

and we ascribe the temperature change due to transport change to the first term, written as

$$\delta T_A = \frac{\delta A}{4\sigma T^3 - \delta B/\delta T} = \frac{-(\delta R + \delta B)}{4\sigma T^3 - \delta B/\delta T} \quad (5)$$

This estimate of δT_A , SST change due to the change in the oceanic advective heat flux, is displayed in Fig. 7a. Since the slab ocean model does not include ocean dynamics, $\delta T_A = 0$ in that case. The pattern of δT_A bears a visual resemblance to the CLIMAP δT (see Fig. 3c, d) extending even to the sign. It also shows a resemblance in spatial distribution to LGMC δT (Fig. 3a) which broadly represents the overall cooling superimposed on δT_A . These results clearly suggest that δA plays a major role in determining the SST response.

To illustrate the processes contributing to the change in δT_A , we plot the change in the oceanic heat flux for the LGMC simulation in Fig. 7b obtained from $\delta A \equiv -(\delta R + \delta B)$. We also estimate the horizontal ($\delta A_H = C_*\delta(\mathbf{v} \cdot \nabla T)$, where $C_* = \rho_0 C_p h$ and ρ_0 is the reference density, C_p the specific heat of sea water, and h the thickness of the upper layer) and

vertical ($\delta A_V = C_*\delta(w \frac{\partial T}{\partial z})$) components of the change in upper ocean heat transport derived from ocean model output in Fig. 7c, d.

Figure 7 indicates that the cooling in the tropical Pacific, north-eastern Atlantic, subtropical Pacific, and the southern tip of Africa, and the warming in the north- and southwestern Pacific and Atlantic, and over the Southern Ocean (Fig. 7a) are due primarily to the change in horizontal heat transport δA_H (Fig. 7c). The change in the vertical heat transport (Fig. 7d) overall plays a relatively minor role in the SST change, except for the equatorial regions where δA_V somewhat contributes to the change in the surface temperature.

Mismatches between δA (Fig. 7b) and $\delta A_H + \delta A_V$ (Fig. 7c plus 7d) found, for example, in the equatorial Pacific, northern North Atlantic, and the Southern Ocean, are presumably due to diffusion and convection processes not included in the calculation of δA_H and δA_V . In the northern North Atlantic the strong negative heat flux anomaly found in δA but not obvious in δA_H or δA_V is apparently associated with a reduction in deep convection, while in the Southern Ocean the positive heat flux anomaly in δA is largely due to an enhanced convection.

Comparing Fig. 7a with Fig. 3a indicates that in the central equatorial Pacific and the northeastern Atlantic

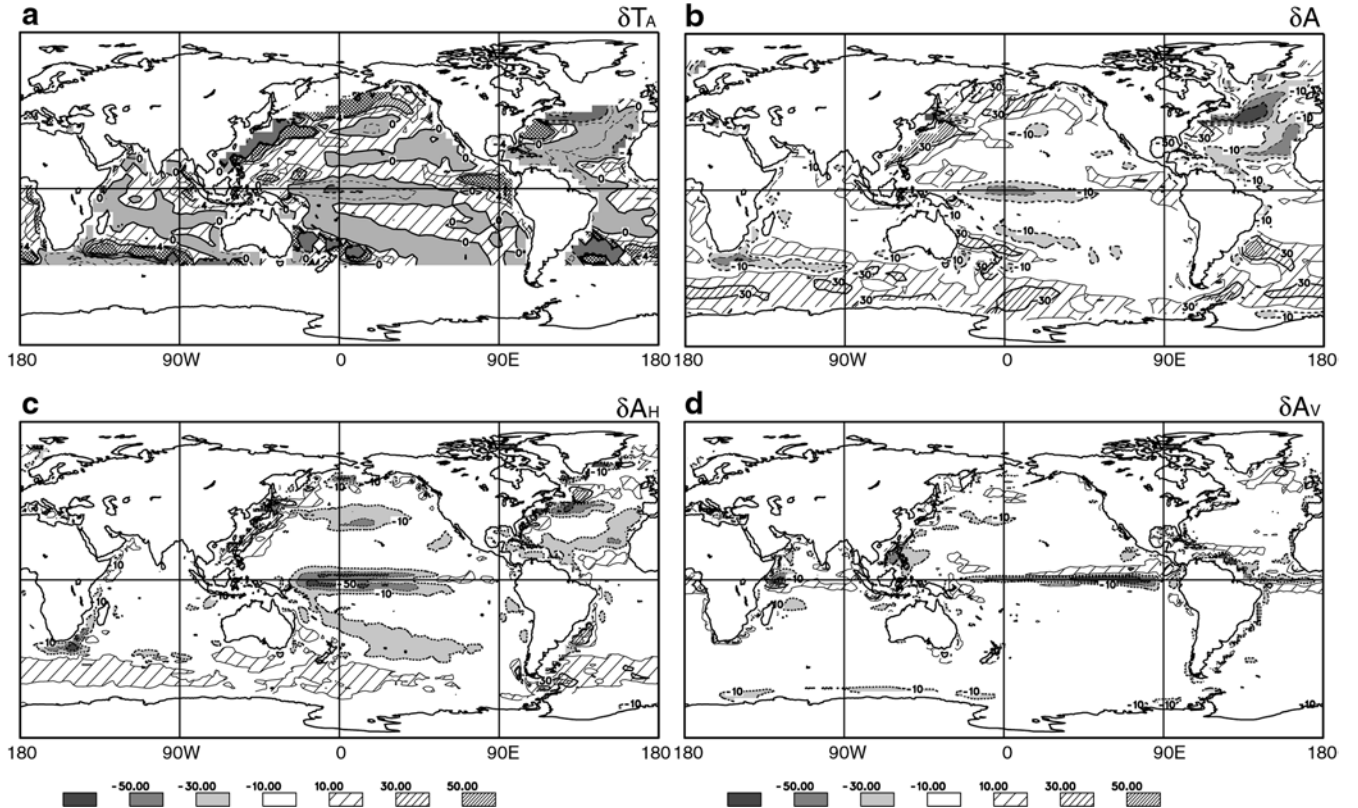


Fig. 7 Geographic distribution of the change in, **a** surface temperature due to advective heat flux, **b** annual-mean oceanic advective heat flux from $-(\delta R + \delta B)$, **c** estimated oceanic horizontal heat flux, and **d** estimated oceanic vertical heat flux at

the surface layer. No data are shown in regions where Eq. (5) is invalid due to presence of sea ice or large $\partial T/\partial t$. Contour intervals are 2 °C for temperature and 20 W m⁻² for heat fluxes

the change in ocean advection accounts for at least half of total SST change. The change in ocean dynamics redistributes heat and plays a critical role in determining the pattern of the SST change.

5.3 Hydrological cycle

Many lines of paleoclimate proxy evidence suggest that it was generally drier during the LGM (see Crowley and North 1991 for review). An overall drier LGM climate is consistent with an increase in atmospheric dust concentration recorded in the Greenland and Antarctic ice cores (Petit et al. 1981) and an increase in wind-blown eolian sediments in deep sea cores (Sarnthein et al. 1981). In both the coupled model and the slab ocean version of the model, the global hydrological cycle weakens as the surface temperature decreases. As shown in Fig. 8, the larger cooling in the LGMC simulation leads to a larger decrease of global mean precipitation (P) and evaporation (E) (15%) than in the LGMM simulation (10%). The latitudinal pattern of the change in the zonal mean hydrological budget is broadly similar in both model versions. In the LGMC simulation, precipitation decreases markedly at three distinct latitude bands, i.e., near the equator associated with a weakening of the ITCZ, in the NH between 50° and 70°N associated with the presence of the continental ice sheet, and at southern high latitudes.

In contrast to the precipitation change, the evaporation change displays a marked inter-hemispheric asymmetry, with the large decrease at northern mid-latitudes associated with the temperature decrease over the ice sheet. Although precipitation and evaporation both decrease in general, the change in $P-E$ shows regions of both increase and decrease. The wetter mid-latitude and more arid tropical and high-latitude climate in the LGMC simulation affects the freshwater flux to the ocean as described later.

The difference in the geographic distributions of P and E between LGM and control simulations in the two model versions is displayed in Fig. 9. In the LGMC simulation, the visually most distinct feature in the precipitation change is the La Niña-like pattern with decreased precipitation in the central Pacific, and increased precipitation in the western Pacific. This is associated with a change in the Walker circulation which is enhanced and extends farther into the western Pacific (not shown). Atmospheric convection regions are shifted westward. This response is the reverse of that occurring under simulated global warming as described in Yu and Boer (2002). The absence of ocean dynamics in the LGMM simulation precludes such a response and the resulting precipitation change pattern is quite different with more precipitation in the central and less in the western part of the Pacific. A major reduction of precipitation over the North American and European ice sheets is seen in both simulations.

The overall cooling results in a reduction in the evaporation almost everywhere with the largest

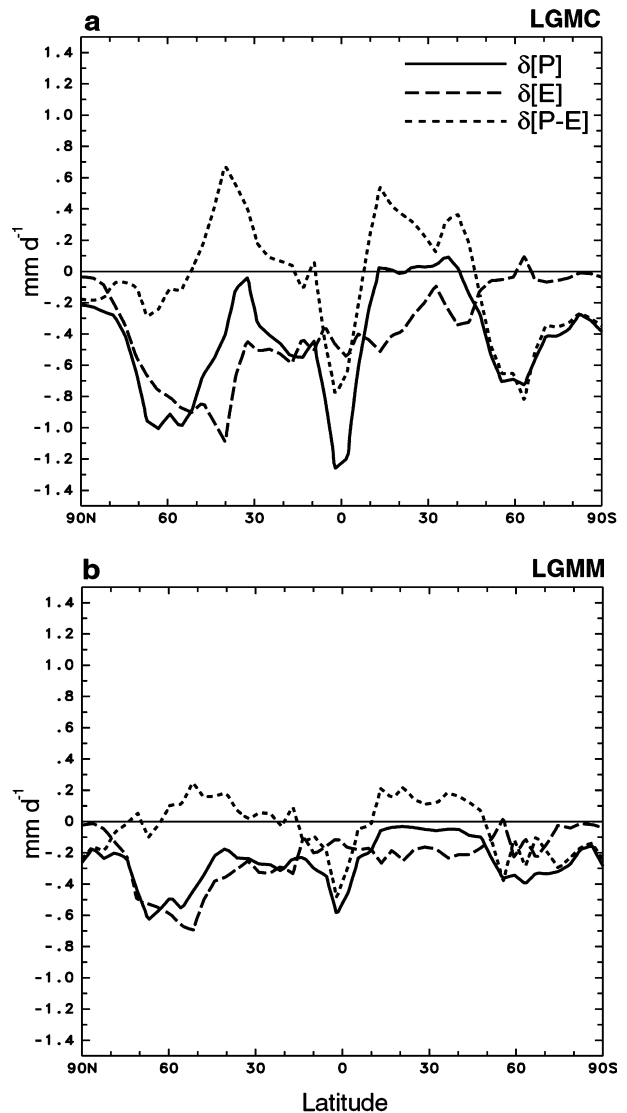


Fig. 8 Latitudinal profile of the change in zonally averaged precipitation (*solid*), evaporation (*dashed*), and $P-E$ (*dotted*) simulated in the, **a** coupled model, and **b** slab ocean model. Units mm day^{-1}

reduction over the continental ice sheets in both models. A stronger reduction in the evaporation than in the slab ocean version is noticeable in the North Atlantic. The comparatively featureless pattern of temperature change over the mid-low latitude ocean in the LGMM simulation (Fig. 3b) is paralleled in the evaporation change (Fig. 9d) while the structure in the LGMC temperature change associated with ocean dynamics is paralleled by structure in evaporation change over the ocean (Figs. 3a and 9c).

Some evidence of the geographical pattern of the hydrological changes over land is available from lake-level data (Street-Perrott et al. 1989; Farrera et al. 1999; Kohfeld and Harrison 2000). The reconstructions suggest that tropical land areas were generally drier during the LGM, while the subtropical land areas were generally wetter. In particular, western USA, the region

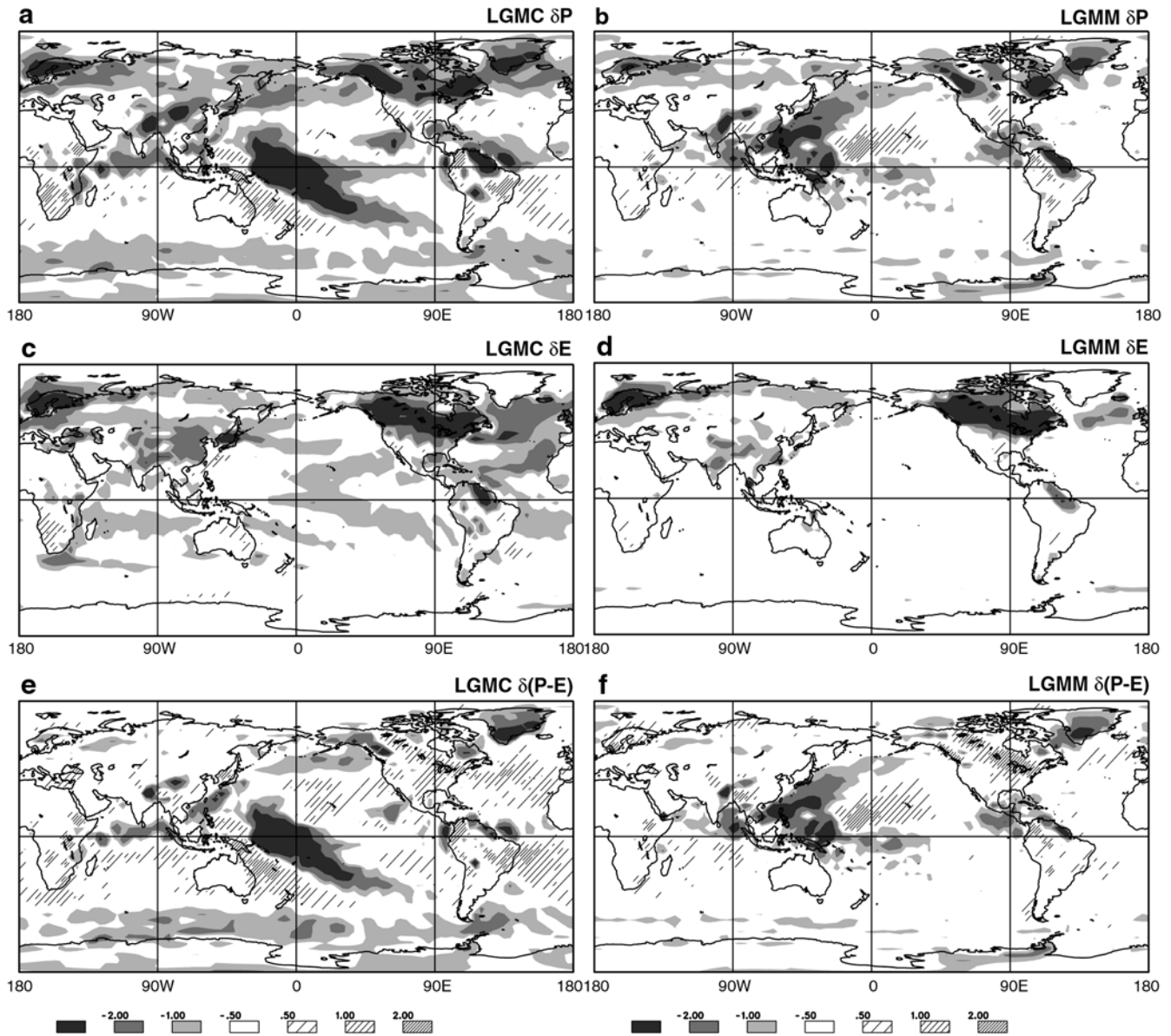


Fig. 9 Geographic distribution of the change in annual-mean precipitation simulated in the, **a** coupled model, **b** slab ocean model; evaporation in the, **c** coupled model, **d** slab ocean model; $P-E$ in the, **e** coupled model, and **f** slab ocean model. Units mm day⁻¹

around Mediterranean Sea, the Middle East, and northwestern Africa were wetter. The change in dust accumulation rate in Greenland and Antarctic ice cores suggests that precipitation decreased by about 50% in high-latitude lands (see Crowley and North 1991 for summary).

There is a broad agreement in the large-scale hydrological budget changes between proxy data and the model simulation. First, in both models tropical regions tend to be drier, while the subtropics to mid-latitude lands are generally wetter in both hemispheres, especially North America (Fig. 9e, f and see Fig. 8). Second, the high latitudes are overall drier in accord with the ice core records. Although both models show broadly similar changes in $P-E$, the LGMC changes are larger in conjunction with the larger changes in temperature

differences over the North Pacific, western Canada, the tropical western Pacific, and eastern Australia.

The $P-E$ change in some land areas influences the change in river discharge. Figure 10 summarizes the discharge from major rivers in the control and LGM simulations. The marked increase in precipitation over evaporation south of the Laurentide ice sheet increases the discharge from the Mississippi river to the North Atlantic from 8.8 to $42.6 \times 10^3 \text{ m}^3 \text{ s}^{-1}$, an increase of more than a factor of 3. The discharge in the North Atlantic from the Amazon river also increases by about a factor of 2.

River discharge decreases markedly in the Arctic due to drier conditions and the accumulation of snow over the ice sheets. Decreases range from about 50% for the Lena to near 100% for the Ob and Yenisey, which are

Fig. 10 Control and LGM river discharge from major drainage basins and percent change. Units $10^3 \text{ m}^3 \text{ s}^{-1}$ and %

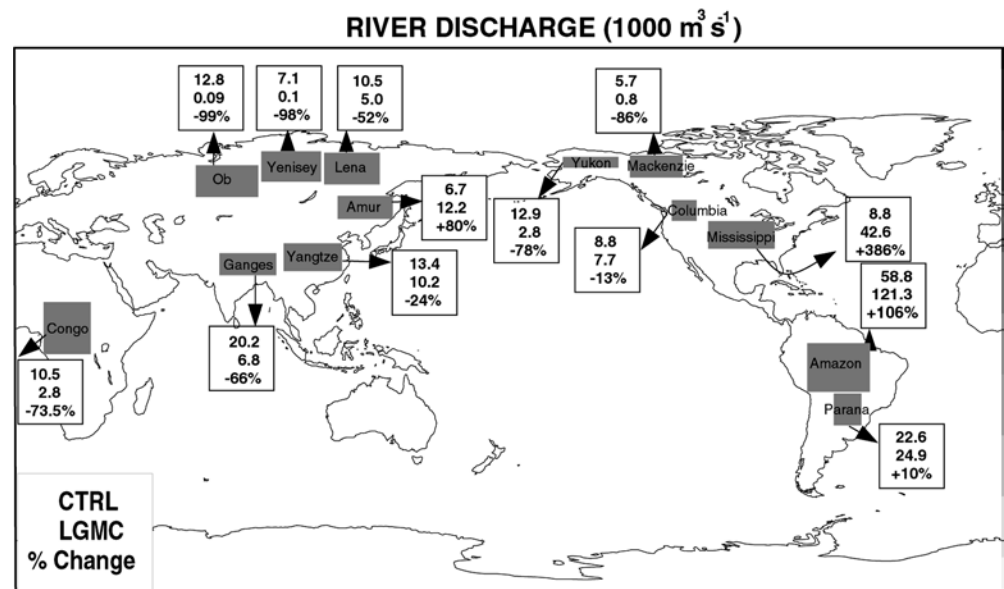
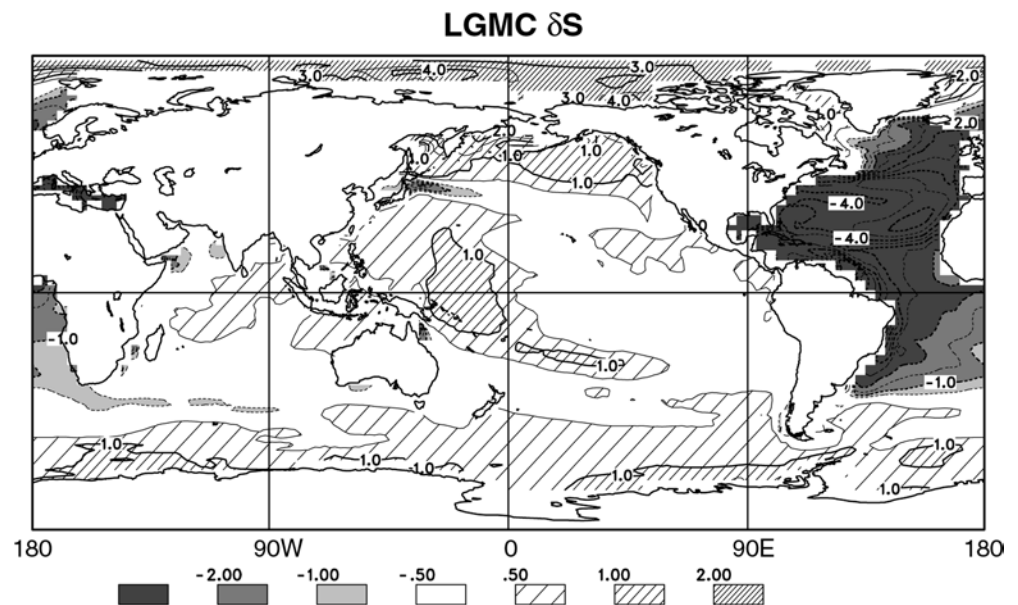


Fig. 11 Geographic distribution of the change in annual-mean sea surface salinity. Contour interval is 0.5 psu



under the influence of the Fennoscandian ice sheet. A marked decrease is also found for the Mackenzie river associated with the Laurentide ice sheet.

In comparison to the Atlantic basin, the river discharge in the Indian and Pacific basins decreases less dramatically. This basin-wise difference in the discharge seems to be due to the relatively weaker $P-E$ change over the Asian continent compared to the American continent (see Fig. 9e). Reliable verification data for the river discharge during the LGM are not available.

The larger surface cooling in the coupled model simulation is accompanied by a more pronounced weakening of the hydrological cycle than occurs in the slab ocean version of the model. The La Niña-like response in the LGM simulation, reflected in the precipitation pattern over the ocean and adjacent lands over the western Pacific, is missing in the LGMM

simulation. The change in the large-scale hydrological budget in both model versions agrees broadly with available proxy evidence. As a consequence of the change in $P-E$, the fresh water flux to the ocean is substantially modified, especially in the North Atlantic and Arctic.

5.4 Surface salinity

Changes in sea surface salinity (SSS) can play a role in long-term climate through a modification of ocean density, convection, the overturning thermohaline circulation, and the associated oceanic meridional heat transport. The SSS change between LGM and control simulations is displayed in Fig. 11 for the LGM case. The SSS changes broadly mirror the changes in $P-E$

(Fig. 9e) with a decrease in the Atlantic and an increase over most of the remainder of the ocean. Figures 9e and 10 indicate that the increase in SSS in the Arctic Ocean is primarily due to a decrease in river discharge. In the tropical western Pacific, SSS increases by about 1 psu due primarily to the decrease in precipitation over the western Pacific associated with the La Niña-like response in agreement with proxy evidence based on the change in $\delta^{18}\text{O}$ (Martinez et al. 1997). The increase in SSS in the North Pacific and over the Southern Ocean is broadly consistent with the reduction in $P-E$.

SSS decreases substantially in the North Atlantic. From a regional reconstruction using dinocyst assemblages, de Vernal et al. (2000) show that SSS was significantly lower in the northern North Atlantic during the LGM consistent with the simulation. The marked decrease in SSS in the North Atlantic has two main causes. The increased fresh water from the Mississippi and Amazon rivers (Fig. 10) is spread over the North Atlantic basin by the Gulf Stream and the gyre circulation. The increase in local precipitation over evaporation also plays an important role in the freshening of the North Atlantic (Fig. 9e). The freshening results in the weakening of the North Atlantic overturning circulation as shown later and the weakened overturning circulation presumably reinforces the freshening of the North Atlantic in association with a decrease in saline water transport to the north. This behavior is found also in Manabe and Stouffer (1988), although not in an LGM context.

The change in hydrological cycle and the associated change in river discharge alter SSS. In particular, the marked decrease in SSS in the northern North Atlantic plays a critical role in LGM climate change via a weakening of the North Atlantic overturning circulation as described in the following section.

5.5 Atmosphere and ocean circulation

5.5.1 Mean sea-level pressure and surface wind

Figure 12 displays the mean sea-level pressure (MSLP) distributions simulated in the control and LGM experiments, and the difference between them for the coupled model. In the LGMC simulation about 1% mass of air is replaced by the volume of ice cap but the global mean MSLP is within 0.1% of that of the control simulation. The control simulation is quite realistic and reproduces the major features of the large-scale climatological circulation. The mean sea-level pressure increases markedly over regions of enhanced ice and snow cover in the LGM. The Aleutian low in the North Pacific is slightly deeper at the LGM but remains in place, whereas the Icelandic low in the North Atlantic shifts slightly southward presumably in association with the ice edge. Over the Southern Ocean, the sea level pressure increases markedly, i.e. the circumpolar trough become weaker.

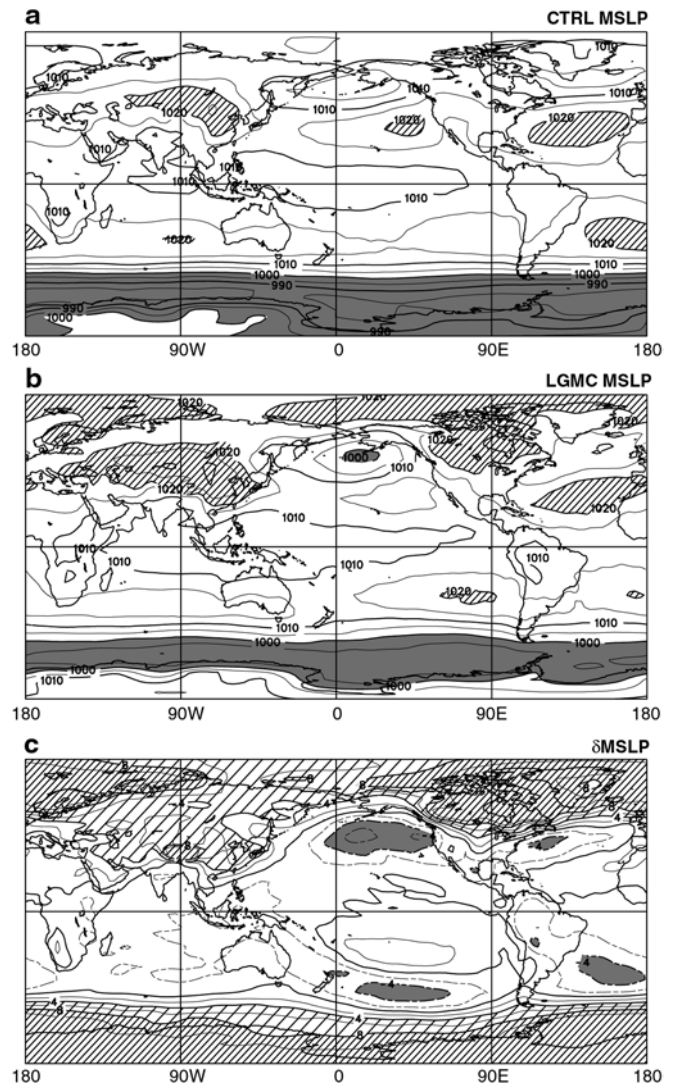
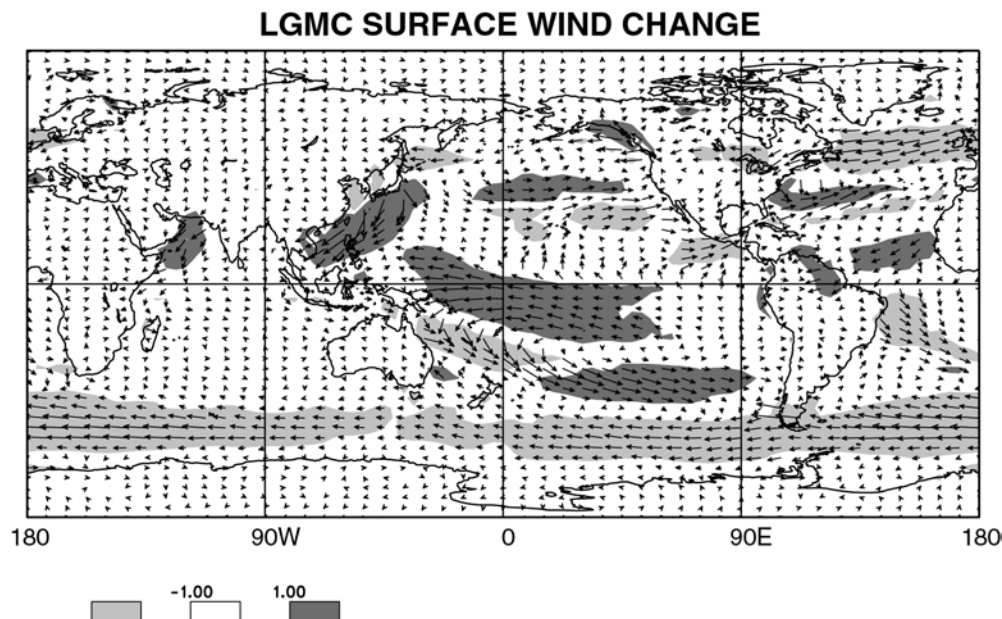


Fig. 12 Geographic distribution of annual-mean sea level pressure for, **a** control, **b** LGM, and **c** change. Contour intervals are 5 hPa for **a** and **b**, and 2 hPa for **c**

Figure 13 shows the geographic distribution of the change in the annual-mean surface winds for the LGMC simulation. The dark shading represents an increase in wind magnitude and the light shading a decrease. Analysis of the seasonal wind change (not shown) indicates that the annual mean change is dominated by the summer season in both hemispheres. In the LGMC simulation, the trade winds are enhanced in the Pacific and Atlantic Ocean. The westerly winds are shifted slightly equatorward in the Pacific and the North Atlantic. The westerly surface winds in the Southern Ocean are reduced by more than 40% due to the suppression of the Antarctic trough and associated weakening of the meridional pressure gradient.

The distribution of windblown (eolian) sediments from deep-sea cores suggests an increase of about 30% for the North Pacific trades and about 50% for the North Atlantic trades and upwelling indices along the

Fig. 13 Geographic distribution of the change in annual-mean surface wind vectors and their magnitude. Dark shading represents an increase and light shading a decrease in the LGM. Units in m s^{-1} .



Peru represent a 30–50% increase in the South Pacific trades (Molina-Cruz 1977; Sarnthein et al. 1981; see Crowley and North 1991 for review). The increase in LGM trade winds in the simulation is consistent with the proxy evidence.

The eolian sediment record (Janecek and Rea 1985) suggests an increase of about 20% for the North Pacific westerly winds and the marked increase in the loess sedimentation rate in Western Europe (Antoine et al. 2001) implies enhanced westerly winds over the Europe during the LGM, while the model results show regions of increased winds in the Pacific and Atlantic but they are accompanied also by regions of decrease. Overall, however, simulated westerly winds decrease. The broad increase in MSLP at high latitudes associated with the Laurentide and Fennoscandian ice sheet means that westerly winds generally decrease in the NH and this result is obtained in other LGM simulations (Gates 1976; Kutzbach and Guetter 1986; Kitoh et al. 2001).

The higher dust concentrations, including sea-salt chlorides, recorded in Antarctic ice cores (74°S, 124°E; 78°S, 106°E) imply a drier climate combined with enhanced atmospheric circulation in the southern high latitudes (Petit et al. 1981; DeAngelis et al. 1987), whereas the LGMc simulation exhibits a significant reduction of SH westerly winds. In the SH, the simulations are less consistent. For example, in an LGM experiment, Gates (1976) obtained a change in Southern Ocean mean sea-level pressure similar to our result, whereas Kutzbach and Guetter (1986) and Kitoh et al. (2001) exhibited slightly enhanced surface winds over the Southern Ocean.

The situation with respect to wind change remains uncertain. There is uncertainty in linking eolian sediments or dust concentration directly to the change in surface winds and the proxy records are generally highly localized and are not representative for the large-scale

surface wind pattern. Overall, the westerly winds in the LGMc simulation are shifted slightly equatorward that yields regions of both increase and decrease. This result disagrees in part with the proxy records, but is consistent with other LGM simulations, especially in the NH. The trade winds are enhanced in the Pacific and Atlantic Ocean and this simulation is consistent with proxy evidence.

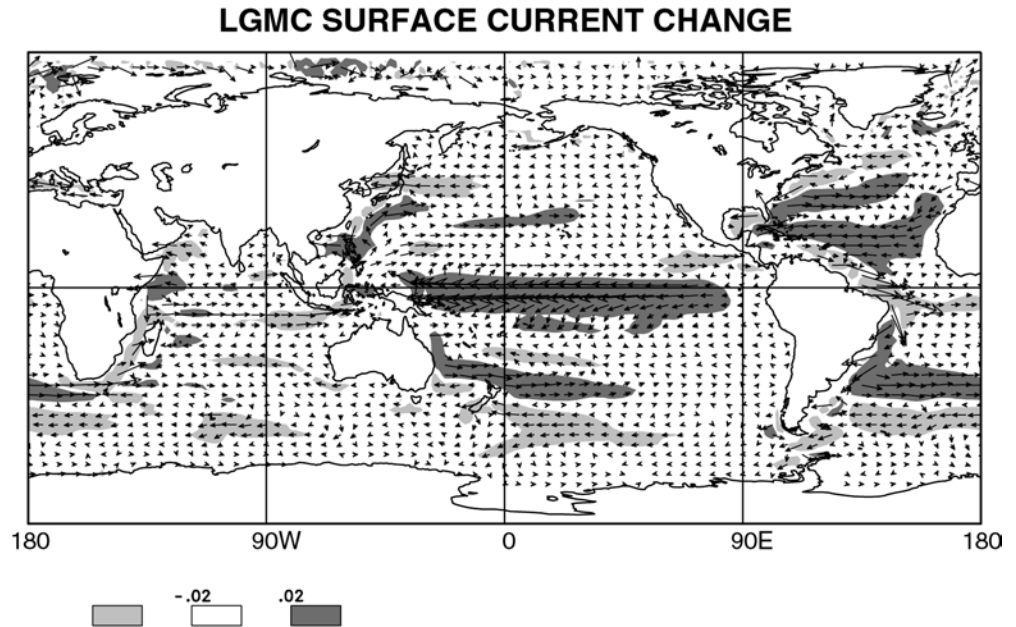
5.5.2 Baroclinic ocean circulation

Figure 14 shows the simulated change in circulation in the upper 50 m of the ocean. The convention for shading is the same as Fig. 13. The change in surface ocean circulation largely parallels that of the change in surface wind of Fig. 13. The most pronounced feature is the marked increase in equatorial currents in the Pacific associated with the mean La Niña-like response. The equatorial current is also enhanced substantially in the North Atlantic. The enhancement of the equatorial currents in the Pacific and Atlantic is consistent with an increase in productivity (Sarnthein et al. 1988) associated with enhanced equatorial upwelling.

The subtropical surface circulation associated with the Gulf Stream, Kuroshio, Brazil, and East Australian currents increase considerably in conjunction with the enhanced surface wind stresses, while a slight decrease is visible in the Antarctic Circumpolar Current regime. In the Indian Ocean the surface ocean currents decrease slightly in general, in particular the Mozambique and Agulhas currents.

CLIMAP infers the change in ocean circulation from the reconstructed SST distribution. In the North Atlantic, the Gulf Stream is inferred to have shifted slightly southward and the North Atlantic Drift, carrying the warm and saline equatorial water to the sub-Arctic

Fig. 14 The change in annual-mean ocean surface current vectors. Otherwise same as Fig. 13



regions, to have weakened. Similar features are inferred in the North Pacific. The cold patches in the equatorial Pacific and Atlantic, off California, the west coast of North Africa, and the east coast of South America are associated with an increase in surface current and upwelling. These features agree well with the LGMc simulation.

Figure 15 shows the geopotential anomaly of the upper model layer ($\Delta\Phi = \int_{p_1}^{p_2} \alpha dp$, where Φ is the geopotential and α the specific volume anomaly) with respect to 1000 db for the CTRL and LGMc experiments. It is the stream function of the geostrophic circulation $\mathbf{V}_g = f^{-1} \hat{k} \cdot \nabla \times \Phi$. The subtropical and subpolar gyre circulations are visible and the steep slope over the Southern Ocean is associated with the circumpolar flow. The large contribution of the ageostrophic component is found in the western and eastern boundaries.

In the LGM, the subtropical gyre circulation in the North Atlantic is enhanced and the North Atlantic Extension is shifted slightly to the south. This implies a slight equatorward shift of the North Atlantic polar front consistent with the CLIMAP reconstruction. In the North Pacific the geostrophic component of the subtropical gyre circulations is slightly weaker. A generally weaker upper layer geostrophic circulation is also found over the SH, in particular the ACC, whereas in the South Atlantic subtropical gyre circulation is substantially enhanced.

Lynch-Stieglitz et al. (1999) reconstruct a local LGM density across the Florida Strait at depths less than 1000 m using the $\delta^{18}\text{O}$ from the calcite tests of foraminifera and infer weaker density gradients across the Florida Strait. Using the geostrophic method, they estimate that the LGM baroclinic Gulf Stream transport was reduced by about 50%. The LGMc simulation,

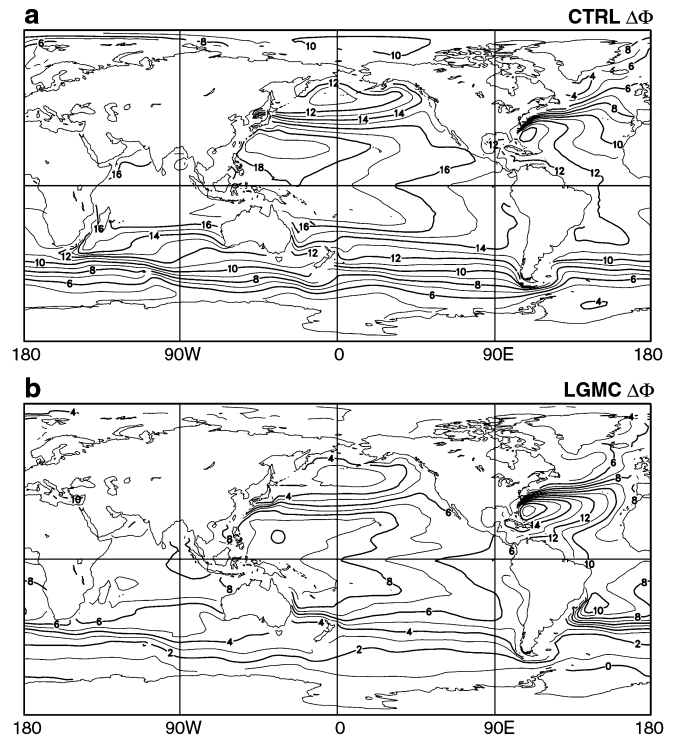


Fig. 15 Geographic distribution of annual-mean surface ocean geopotential anomaly relative to 1,000 db for, **a** control, and **b** LGM. Contour interval is $1 \text{ m}^2 \text{ s}^{-2}$

however, produces a steeper geopotential anomaly gradient in the Gulf Stream region (see Fig. 15) and this implies an enhanced baroclinic circulation associated with the Gulf Stream. This is apparently at odds with the observationally based reconstruction, provided however that the local proxy result is indicative of the overall Gulf Stream change.

5.5.3 Barotropic ocean circulation

The oceanic barotropic stream function Ψ for the CTRL and LGM simulations, and the difference is plotted in Fig. 16. The discussion of the barotropic stream function for CTRL is found in the companion paper (KFBM). In the LGM simulation, the barotropic transport in the North Atlantic and North Pacific subtropical gyre increases by about 10 Sv ($\sim 30\%$) and is displaced slightly southward. The barotropic transport associated with the subtropical gyre in the southern Indian Ocean differs little from the control run, while in the South Pacific it is substantially stronger. The Indonesian Throughflow decreases by about 15%. The ACC transport increases despite the marked decrease in surface wind shown in Sect. 5.5.1. For example, at the Drake Passage the ACC transport increases by about

25% relative to the control run. Since the difference in ACC transport cannot be accounted for by a change in wind stress, we infer that it is mainly due to a change in the bottom pressure torque associated with the change in AABW density.

The steady state horizontal momentum equation may be written to good approximation as

$$f\hat{k} \times \mathbf{v} = -\frac{1}{\rho_0}\nabla p + \frac{1}{\rho_0}\frac{\partial \tau}{\partial z}, \quad (6)$$

where f is the Coriolis parameter, \hat{k} a unit vector in upward direction, ρ_0 the reference density, p pressure, τ horizontal stress. Nonlinear advective terms have been neglected (Holland 1973) as has lateral friction which is not important away from the boundary (Greatbatch et al. 1991). Vertical integration gives

$$f\hat{k} \times \mathbf{V} = -\frac{1}{\rho_0}\nabla P + \frac{1}{\rho_0}p_b\nabla H + \frac{1}{\rho_0}\tau_s, \quad (7)$$

where $\mathbf{V} = \int_{-H}^0 \mathbf{v} dz$, $\mathbf{P} = \int_{-H}^0 p dz$, H the ocean depth, p_b the bottom pressure, and the bottom stress τ_b has been neglected. Taking the curl of Eq. (7) produces the vorticity equation

$$\frac{\beta}{a \cos \varphi} \frac{\partial \Psi}{\partial \lambda} \cong \frac{1}{\rho_0} \hat{k} \cdot \nabla p_b \times \nabla H + \frac{1}{\rho_0} \hat{k} \cdot \nabla \times \tau_s, \quad (8)$$

where $\beta = \frac{df}{d\varphi}$, a the radius of Earth, φ the latitude, λ the longitude. Equation (8) illustrates that the vorticity is largely balanced by bottom pressure torque and wind stress curl.

Figure 17 displays the terms in Eq. (8) for the control experiment and their differences in the LGM run. The vorticity and wind stress curl terms are calculated directly and the bottom pressure torque term is estimated indirectly as their difference. In the control run, the wind stress curl is dominant in the mid-latitude gyres (as expected), while in the western boundary regions and over the Southern Ocean the inferred bottom pressure torque dominates. The bottom pressure torque in the control run (Fig. 17c) is broadly consistent in spatial pattern and magnitude with that obtained in a recent high resolution OGCM (Hughes and De Cuevas 2001).

The broad agreement and high spatial correlation ($>90\%$) between Fig. 17d and 17f suggest the critical role of bottom pressure torque in the change in the barotropic stream function in the LGM. This is particularly noticeable in the western boundaries and over the Southern Ocean. The change in the bottom pressure torque reflects changes in the density of deep and bottom water masses. The change in surface stress torque contributes in the mid eastern Pacific.

To summarize, the barotropic stream function associated with the subtropical gyres in the North Atlantic and Pacific increases by about 30% and the ACC volume transport increases by about 25% in the LGM. The change in bottom pressure torque due to a change in density structure plays the main role in modifying the

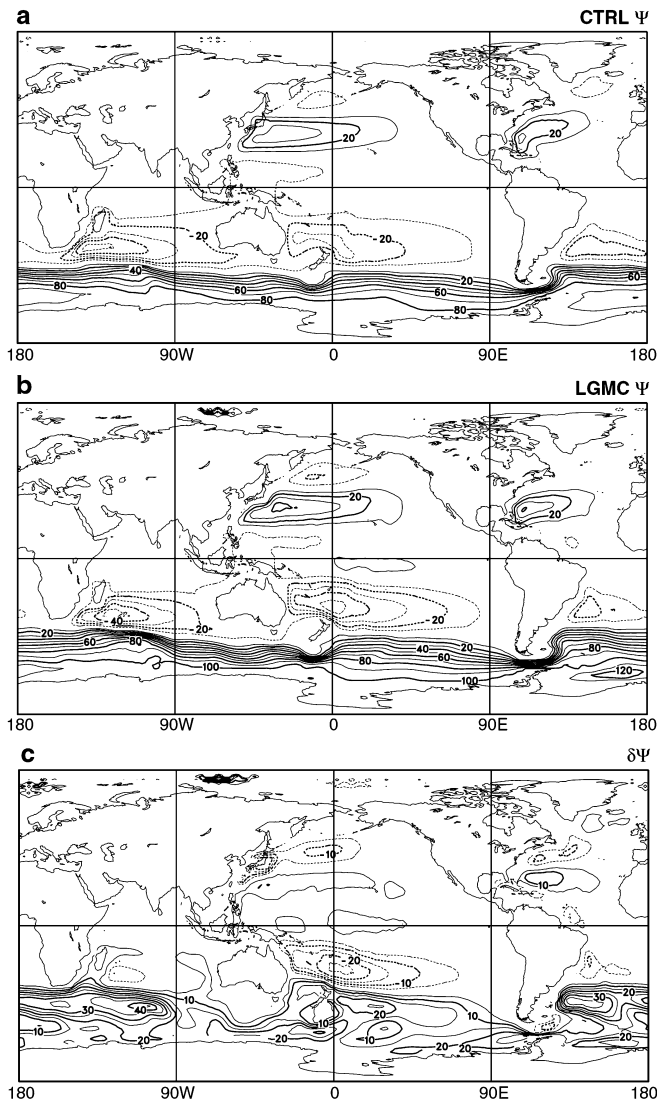


Fig. 16. Geographic distribution of annual-mean barotropic stream function for, **a** control, **b** LGM, and **c** change. Units Sv ($10^6 \text{ m}^3 \text{ s}^{-1}$)

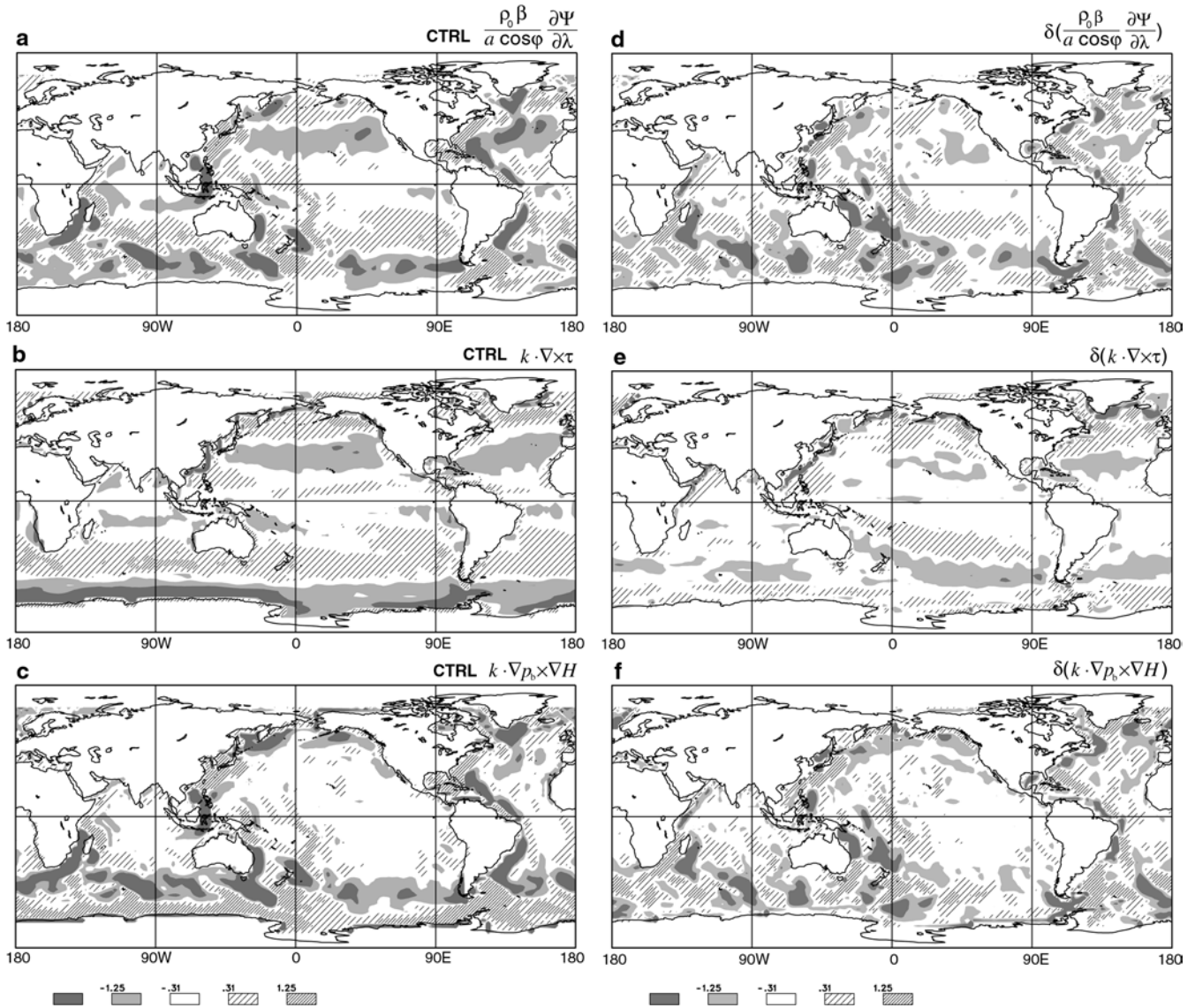


Fig. 17 Geographic distribution of the terms in barotropic vorticity Eq. (8) simulated in control for, **a** vorticity, **b** wind stress curl, **c** inferred bottom pressure torque; the change for, **d** vorticity, **e** wind stress curl, and **f** inferred bottom pressure torque. Units 10^{-7} N m^{-3}

barotropic stream function in the LGM, with changes in the wind stress curl of lesser importance.

5.5.4 Meridional overturning ocean circulation

Figure 18 displays the meridional overturning stream functions for the control and LGM simulation for global and Atlantic domains. In the global domain, the formation and outflow of NADW and North Pacific Intermediate Water (NPIW) is reflected in the large positive overturning circulation cell in the NH. The outflow of AABW is represented as the negative overturning cell in the deep ocean below 3000 m. The strong positive cell at about 50°S , the Deacon cell, is driven by Ekman divergence in response to the westerlies over the

Southern Ocean. The eddy induced ‘bolus’ velocity in the GM scheme, which counters the Deacon cell, is not included in the stream function. The negative cell near the Antarctic boundary is associated with the formation of AABW.

The maximum of the global overturning stream function in the NH is about 12 Sv in the CTRL which diminishes to about 6 Sv in the LGMC simulation. The overturning stream function associated with the AABW formation is much larger (~ 16 Sv) in LGMC compared to about 2 Sv in CTRL. This is due to enhanced convection in the Southern Ocean presumably as a result of reduced water column stability associated with increased SSS and decreased SST as shown earlier. In response to the marked reduction in the strength of the overturning circulation in the NH, the overturning circulation

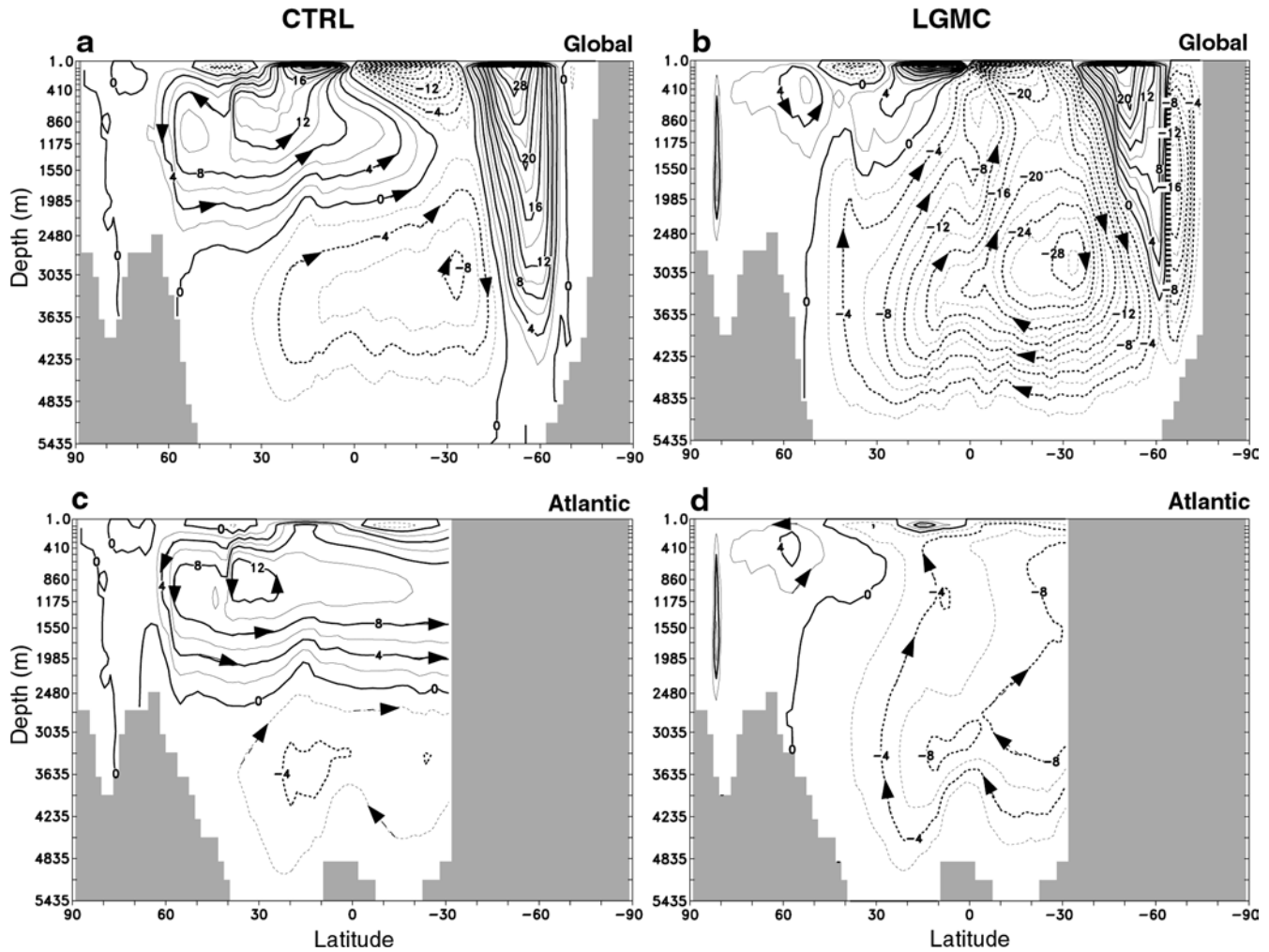


Fig. 18 Annual-mean meridional stream function for the global domain in, **a** control, **b** LGM; for the Atlantic in, **c** control, and **d** LGM. Contour interval is 2 Sv

associated with the AABW outflow predominates the global ocean domain (Fig. 18b).

The proxy estimates of AABW production differ considerably. Some authors suggest that the production of AABW decreased during the LGM (Ledbetter 1984), whereas Hall et al. (2001) estimate the intensity of the glacial deep Pacific western boundary current using various proxies and obtain a significantly enhanced deep Pacific throughflow which is closely linked to the rate of AABW production. Though the rate of AABW formation is not clear, a general agreement is that the NH sources were diminished during the LGM and the deep ocean basins were filled with the water originating in the Southern Ocean (Boyle and Keigwin 1982, 1987; Duplessy et al. 1988; Oppo and Fairbanks 1987).

In the Atlantic domain, the maximum overturning stream function associated with the NADW production is about 10 Sv in CTRL (Fig. 18c). In the early part of the simulation with LGM forcing conditions, the North Atlantic overturning circulation was quite vigorous as a result of intensified oceanic deep convection. The North Atlantic convection subsequently decreases in response

to the increase in fresh water supply. By the end of the simulation deep convection has largely shut down and the maximum of the North Atlantic overturning stream function is about 4 Sv (40% of what it was in the control run) (Fig. 1). In the LGMC simulation, the NADW outflow is much shallower than that of CTRL (like intermediate water rather than deep water) and is limited to the north of 30°N (Fig. 18d). As in the case of the global domain, the Atlantic basin is composed of the water originated in the Southern Ocean due to the much weaker role of the NADW formation and outflow.

Based on $\delta^{13}\text{C}$ variations in benthic foraminifera and using geochemical proxy data various authors suggest that the NADW production was generally weaker (Table 2) and shallower than present. Some authors refer to “glacial north Atlantic intermediate water” (GNAIW) (e.g., Duplessy et al. 1988) and some evidence indicates that GNAIW was not exported to the Southern Ocean (e.g., Oppo and Horowitz 2000), consistent with our model result. On the other hand, some proxies such as Cd/Ca, Ba/Ca, Pa/Th ratios indicate that the NADW production decreased only slightly (Boyle 1992)

Table 2 Observed and simulated North Atlantic Deep Water production in the LGM. Bold face indicates proxy records

Production	Method/model	References
Reduced	$\delta^{18}\text{O}$ Cd/Ca and $\delta^{13}\text{C}$ $\delta^{13}\text{C}$	Duplessy et al. (1980) Boyle and Keigwin (1982, 1987); Oppo and Horowitz (2000) Curry and Lohman (1982); Oppo and Fairbanks (1987); Duplessy et al. (1988); Curry et al. (1988); Sarnthein et al. (1994)
	Neodymium EMBM + OGCM Zonal mean OGCM <i>CCMa coupled model</i>	Rutberg et al. (2000) Weaver et al. (1998) Fichefet et al. (1994) <i>This simulation</i>
Slightly reduced	Cd/Ca Simple AGCM + Zonal Mean OGCM	Boyle (1992); Oppo and Rosenthal (1994) Ganopolski et al. (1998)
Similar to present	Pa/Th	Yu et al. (1996)
Increased	UKMO coupled model MRI coupled model	Hewitt et al. (2001) Kitoh et al. (2001)

or was similar to present and NADW was actively exported to the Southern Ocean (e.g., Yu et al. 1996).

Model studies also exhibit various results. Using coupled models of intermediate complexity, Ganopolski et al. (1998) obtained a maximum North Atlantic overturning circulation similar to that of their control value but with slightly shallower outflow, while Weaver et al. (1998) found a much weaker (by about 50%) and shallower North Atlantic overturning circulation than their control run. Using a zonally averaged OGCM, Fichefet et al. (1994) also obtained a North Atlantic overturning cell that was reduced by about 40%. These results are generally consistent with our simulation. In more recent LGM simulations using coupled models, on the other hand, Hewitt et al. (2001) and Kitoh et al. (2001) obtain an increase in maximum North Atlantic overturning of $\sim 25\%$ and vigorous outflow to the south.

Although many lines of proxy evidence have shown that the North Atlantic overturning circulation was much weaker and shallower during the LGM, the cause for these changes has not been clear. Figure 19a displays the net change in surface density in the North Atlantic. In the northern North Atlantic, surface density decreases by about 0.5 to 1.0 kg m^{-3} in the LGM. To examine what caused this change, we distinguish the change in surface density due to the change in SSS and SST (Fig. 19b, c). The substantial decrease in surface density due to the reduction in SSS outweighs the slight increase in density due to the reduction in SST. By contrast, in the Hewitt et al. (2001) result a reduction in $P-E$ together with the reduction in surface temperature results in an increase in the overturning circulation. Our result indicates that the weakening of the North Atlantic overturning during the LGM was caused by a reduction of SSS through a larger supply of fresh water to the North Atlantic basin from the Mississippi and Amazon rivers and by an increase in $P-E$ over the North Atlantic as illustrated in Sect. 5.3.

5.6 Meridional heat transport

The change in the ocean temperature and circulation alters the oceanic meridional heat transport. The vertically integrated and zonally and time averaged heat transport in the model is

$$\Gamma(\varphi) = 2\pi a \cos \varphi \int_{-H}^0 \rho_0 C_p [\overline{vT} + \overline{D}] dz = \Gamma_A + \Gamma_D, \quad (9)$$

where ρ_0 is the representative ocean density, C_p the specific heat of sea water, \overline{vT} is the resolved advection and \overline{D} represents the parametrized subgrid diffusive heat flux. The advective part Γ_A can be further decomposed as

$$[\overline{vT}] = [\overline{v}][\overline{T}] + [\overline{v}^* \overline{T}^*] + [\overline{v'} \overline{T'}], \quad (10)$$

where the square bracket represents the zonal mean, the overbar the time mean, the star the departure from the zonal mean, and the prime the departure from the time mean. The first term in the right-hand side of Eq. (10) is associated with the stationary meridional overturning circulation, the second term the stationary eddy (gyre) circulation, and the third term the transient eddies. The term associated with transient eddies is generally small and is not resolved because we use temporally averaged model output in the calculation. The zonal-mean meridional velocity includes the eddy-induced tracer transport velocity from the GM parametrization. The diffusive heat transport Γ_D is obtained as the difference between the advective component Γ_A of the heat transport in Eq. (10) and the total heat transport estimated from an indirect method by integrating the net heat flux (h) into the ocean ($\Gamma_I(\varphi) = 2\pi a^2 \int_{-\pi/2}^{\varphi} [\overline{h}] \cos \varphi d\varphi$) assuming near equilibrium, i.e. $\Gamma_D = \Gamma_I - \Gamma_A$.

Simulated heat transport components are displayed in Fig. 20 where the total heat transport is obtained indirectly from heat storage and fluxes across the

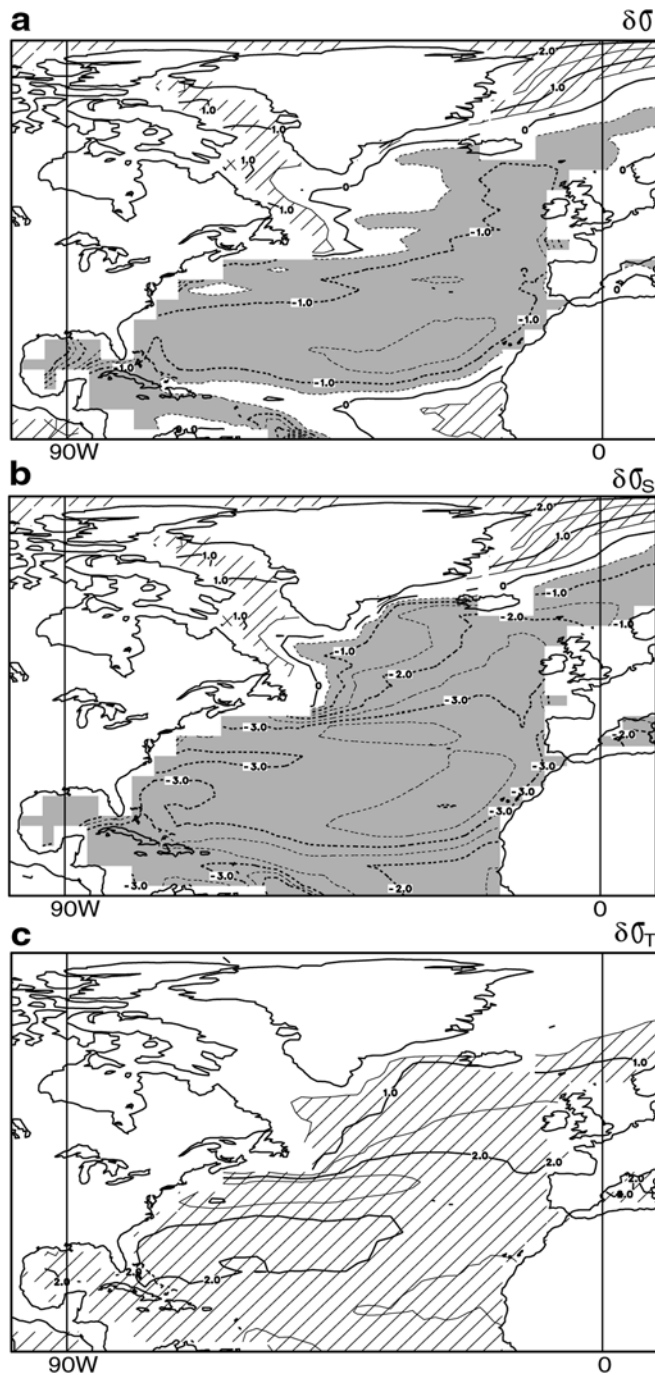


Fig. 19 Geographic distribution of the change in annual-mean, **a** ocean surface density in the North Atlantic; density change due to a change in, **b** SSS, and **c** SST. Contour interval is 0.5 kg m^{-3}

surface. The meridional ocean heat transport for the CTRL simulation is in broad agreement with observed estimates (KFBM). The largest contribution is due to the meridional overturning circulation followed by the gyre component in which the relative maxima found between 30° – 40° and at about 50° in both hemispheres are due to the subtropical and subpolar gyres. The diffusive heat transport in CTRL is relatively small everywhere except at about 45°S where a relative

maximum is associated with the strong gradients at the Antarctic polar front.

The weakening of the North Atlantic overturning circulation results in the reduction of northward heat transport by about 0.8 PW in the LGM (Fig. 20b). However, this is somewhat offset by the slight increase in northward heat transport due to the change in the gyre and diffusion ($\sim 0.3 \text{ PW}$), resulting in the net decrease in the northward heat flux by about 0.5 PW (about 30%) (Fig. 20a). The difference in total transport is everywhere negative and this represents a decrease in poleward heat transport in the NH but an increase in the SH. The reverse happens in the SH, where the change in the meridional overturning dominates the increase in the southward heat transport compared to the decrease in the heat transport due to the gyre and diffusion. In the SH, the intensified overturning circulation transfers about 40% more heat toward the south in the LGM.

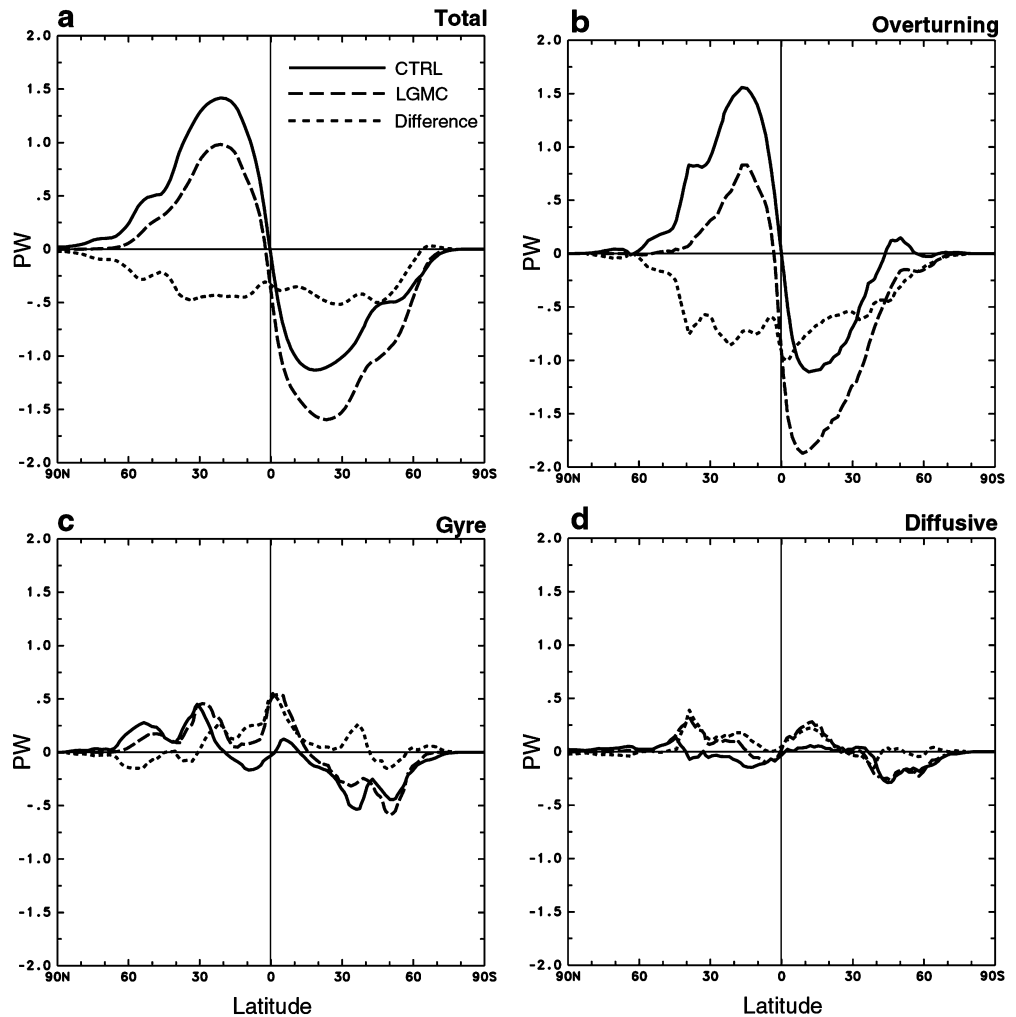
There is no proxy evidence for the change in oceanic heat transport during the LGM. However, a much weaker North Atlantic overturning and cooler deep ocean, supported by many lines of proxy evidence, imply that the LGM poleward heat transport pattern was similar to that obtained in the coupled model simulation. The decrease in northward heat transport simulated here agrees with results from studies based on simpler models (Weaver et al. 1998; Fichefet et al. 1994), but contrasts with the coupled model results of Hewitt et al. (2001) who obtained an increase in northward heat transport due to the stronger meridional overturning circulation in their LGM simulation.

5.7 Sea ice

NH sea-ice cover expands during the simulation and the area considerably exceeds that of the control run by the end of the simulation. In the SH sea-ice cover decreases remarkably during the first century (Fig. 1e) due to enhanced oceanic convection and the associated upward flux of heat as described in KFBM. As the deep ocean cools (Fig. 5) convection slows and the Antarctic sea ice cover slowly recovers until it exceeds the control run values.

Figure 21 shows the geographic distributions of sea-ice thickness in February for the NH and August for the SH for the control run and the LGM experiment. The regions where land replaced ocean in the LGM are indicated by hatching. Figures 21e, f displays sea-ice cover from CLIMAP (1981). The perennial sea-ice cover, represented by thick lines in each figure, increases in the LGM in the simulation as well as in the CLIMAP (1981) reconstruction. The CLIMAP (1981) reconstruction suggests that the sea ice extended to about 50°N in the NH covering the whole Norwegian Sea (Fig. 21e), whereas more recent works suggest that the Norwegian Sea was seasonally ice free (Weinelt et al. 1996; de Vernal 2000). In the SH the sea-ice

Fig. 20 Zonally integrated annual-mean meridional ocean heat transport components simulated in CTRL (*solid*), LGMC (*dashed*), and difference between the two experiments (*dotted*) for, **a** total, **b** meridional overturning, **c** gyre, and **d** an estimate of diffusion. Units PW (10^{15} watt)



margin extended equatorward by about 10° in the Pacific sector and by about 12° – 15° in the Indian-Atlantic sectors relative to the present sea-ice margin (Fig. 21f). This represents an approximate doubling of the area of Antarctic ice cover.

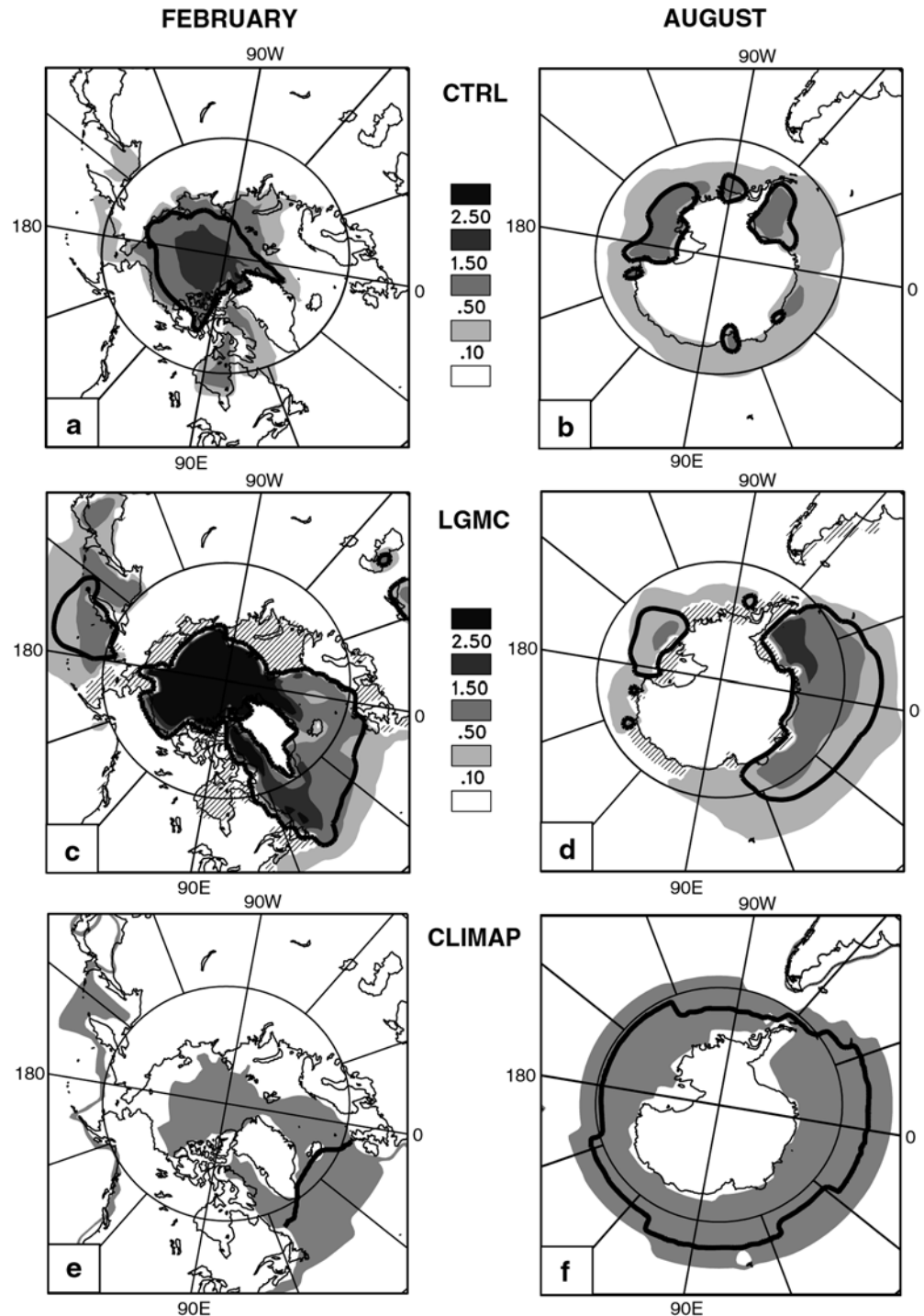
In comparison to the CLIMAP (1981) and other more recent reconstructions, the sea-ice coverage in the LGMC simulation is greater in the NH but considerably less in the SH, mainly in the Pacific sector. In the NH, the increase of the simulated sea ice is apparently associated with the decrease in northward heat transport as a consequence of the weakening of the North Atlantic overturning circulation described. The reverse is apparently the case in the SH although sea-ice cover is not yet in equilibrium (Fig. 1).

It is difficult to know to what extent the mismatch between simulated and reconstructed sea-ice cover is a failing of the simulation. There is considerable uncertainty in the sea-ice edge location estimated by CLIMAP (Crowley and Parkinson 1988). CLIMAP used the change in sedimentological boundaries to estimate the LGM sea-ice margin and Burckle et al. (1982) discuss some difficulties with this approach.

6 Summary and conclusions

We explore the response of the CCCma coupled climate model (CGCM2) to the imposition of LGM conditions including a reduction in CO_2 concentration, ice sheet topography, and changes in land boundaries. The modelled climate system initially undergoes a rapid adjustment process, which is described in some detail in Kim et al. (2002). After this initial rapid adjustment period during the first century of the simulation, the slower approach to the LGM climate is simulated using a periodically synchronous coupling technique. After 900 years the system is approaching equilibrium, although some quantities continue to adjust even at this time. The results of the coupled integration (LGMC) are analyzed and compared with CLIMAP and other proxy data and contrasted with the LGM simulation using a mixed layer (slab) ocean component (LGMM) described in Vettoretti et al. (2000). The main focus of this study is to investigate how the climate system operates under glacial conditions including the role of ocean dynamics in the LGM climate.

Fig. 21 Geographic distribution of sea ice thickness in control for, **a** NH February, **b** SH August; in LGM for, **c** NH February, **d** SH August; LGM sea-ice extent reconstructed in CLIMAP (1981) for, **e** NH February, **f** SH August. In the model results, the areas changed to land in the LGM are represented by *hatching*. *Thick lines* represent perennial sea-ice cover. Units in meters



The global mean surface air temperature (SAT) and sea surface temperature (SST) decrease by about 10 °C and 5.6 °C in the coupled model. These temperature changes are larger than in the slab ocean version (6.3 and 3.8 °C). The difference in surface temperature response between the two model versions is necessarily a result of coupled and ocean feedback processes which operate in the coupled model but which are absent in the slab ocean model. Tropical SST decreases by 6.5 and

3.3 °C in the coupled model and the slab ocean model, respectively. CLIMAP reconstructions suggest that the tropics cool by only about 1.7 °C and the modelled results are considerably cooler than this. The simulated tropical SST change is in better agreement with more recent proxy estimates, however, which suggest a cooling of more than 5 °C. With the incorporation of a full ocean component, the LGMC simulation gives a more realistic spatial SST pattern than is the case with the slab

ocean component, capturing features associated with ocean dynamics that are seen in the CLIMAP reconstructions.

There are also clear differences in the surface heat budget between the LGMC and LGMM simulations. While there is little difference between the two model versions in the net heat budget over land, over oceans the change in ocean dynamics in the LGMC simulation results in a major modification in the surface heat budget. The change in horizontal heat transport acts to cool the surface in the equatorial Pacific and this accounts for about 50% of total cooling in that region. The change in horizontal heat transport acts to warm the surface layer in the mid-latitude western Pacific and Atlantic associated with an enhanced subtropical gyre circulation, while it acts to cool the surface in the northeastern Atlantic.

The larger decrease of the surface temperature in the coupled model is associated with a larger reduction in global precipitation rate (about 15%) than the slab ocean version (10%). In the coupled model the tropical Pacific warm pool retreats to the west and a mean La Niña-like response is simulated with less precipitation over the central Pacific and more in the western tropical Pacific. The change in the precipitation pattern is, if anything, opposite in the LGMM simulation with a slight increase in the precipitation in the central Pacific and a decrease in the western Pacific.

The change in evaporation is similar over land in both model versions, but again differs over the ocean in association with the more spatially variable SST change in LGMC. The generally drier climate of the LGM means that precipitation and evaporation as well as $P-E$ all decrease in general although there are some oceanic areas, such as in the Atlantic Ocean and the western Pacific, where $P-E$ increases. Increases in $P-E$ over North America and around the Mediterranean reflect a wetter climate in these areas and this is reasonably coincident with proxy estimates.

The more arid ocean climate in the LGM results in an increase in SSS almost everywhere. This is particularly the case in the Arctic Ocean where large SSS increase is due to a decrease in river discharge to the Arctic Ocean associated with the accumulation of snow over the ice sheet. A large increase in SSS is also found in the tropical central Pacific and in the Southern Ocean due to the overall drier ocean climate. The North Atlantic by contrast shows a marked decrease in SSS where values are more than 4 psu lower at the LGM. This remarkable reduction of SSS in the North Atlantic is attributed to an increase in fresh water supply by an increase in discharges from the Mississippi and Amazon rivers and an increase in $P-E$ over the North Atlantic ocean itself. The discharges increase in association with the wetter LGM climate south of the Laurentide ice sheet and in South America.

The trade winds are enhanced and the westerly winds are shifted slightly equatorward. Over the Southern Ocean the westerly winds decrease by more than 40%

due to the weakening of the meridional (equator to pole) pressure gradient associated with larger cooling in the low latitudes than in high latitudes. The enhancement of the trades results in an increase of subtropical ocean surface circulation associated with the Gulf Stream and Kuroshio Current with slight equatorward displacement. The upper layer geostrophic circulation associated with the North Atlantic gyre is also enhanced, whereas in the Pacific and the Southern Ocean it is slightly weaker in the LGM. The barotropic stream function associated with the subtropical gyres in the North Atlantic and Pacific increases by about 30%. The barotropic ACC transport at the Drake Passage increases by about 25% despite weaker zonal wind stress. Analysis indicates that the change in the bottom pressure torque associated with the change in deep and bottom water density is responsible for the increase.

The fresh water capping of the northern North Atlantic results in a marked reduction of deep convection and consequently a marked weakening of the North Atlantic overturning circulation. In the LGM, the maximum overturning stream function associated with the NADW formation decreases by about 60% relative to the control run. The depth of the North Atlantic overturning is also much shallower and its outflow remains north of the equator. This result is supported by many lines of proxy evidence. In the Southern Ocean, oceanic convection is stronger in the LGM due to reduced stratification associated with an increase in SSS and a decrease in SST. The strong convection results in a substantial increase in the overturning stream function associated with the formation of AABW and the outflow. Due to a much weaker role of NADW in the LGM, the AABW outflow dominates deep ocean water mass properties.

There is a 30% decrease in northward ocean heat transport in the NH and a 40% increase in the SH associated with the simulated LGM changes in the overturning circulation. The change in poleward heat transport influences the distribution of sea ice area and thickness which, in the model, are overestimated in the Arctic but considerably underestimated in the Antarctic in comparison to the CLIMAP (1981) and more recent reconstructions.

In conclusion, the LGM climate simulated by the CCCma coupled model agrees with observational proxy evidence in many respects, although proxy results often differ among themselves. In particular, the simulation agrees with data indicating a weaker and shallower North Atlantic overturning and a comparatively large tropical cooling. The analysis illustrates especially the important role of ocean dynamic feedbacks in shaping the spatial distribution and magnitude of climate change associated with LGM conditions.

Acknowledgements We wish to thank CCCma colleagues, especially Warren Lee and Daniel Robitaille for model support, Bernard Miville and Fouad Majaess for technical support, and Steve Lambert for proof reading. Comments by Norman McFarlane, William Merryfield, and John Fyfe have helped to improve the

manuscript and are greatly appreciated. We also thank Dr. Ronald Stouffer and an anonymous reviewer for constructive comments. This study was supported by the Climate System History and Dynamics (CSHD) program and the Canadian Climate Research Network, Climate Variability Project.

References

- Aeschbach-Hertig W, Peeters F, Beyerle U, Kipfer R (2000) Paleotemperature reconstruction from noble gases in ground water taking into account equilibration with entrapped air. *Nature* 405: 1040–1044
- Antoine P, Rousseau D-D, Zöller L, Lang A, Munaut A-V, Hatté C, Fontugne M (2001) High-resolution record of the last Interglacial-glacial cycle in the Nussloch loess-palaeosol sequences, Upper Rhine Area, Germany. *Quat Intl* 76/77: 211–229
- Bard E, Rostek F, Sonzogni C (1997) Interhemispheric synchrony of the last deglaciation inferred from alkenone paleothermometry. *Nature* 385: 707–710
- Barrows TT, Juggins P, Deckker De, Theide J, Martinez JI (2000) Sea-surface temperatures of the southwest Pacific Ocean during the Last Glacial Maximum. *Paleoceanography* 15: 95–109
- Barnola JM, Raynaud D, Korotkevich YS, Lorius C (1987) Vostok ice core provides 160,000-year record of atmospheric CO₂. *Nature* 329: 408–418
- Beck JW, Recy J, Taylor F, Edwards RL, Cabioch G (1997) Abrupt changes in early Holocene tropical sea surface temperature derived from coral records. *Nature* 385: 705–710
- Boer GJ (1993) Climate change and the regulation of the surface moisture and energy budgets. *Clim Dyn* 8: 225–239
- Boer GJ, Lambert SJ (2001) Second-order space-time climate difference statistics. *Clim Dyn* 17: 213–218
- Boer GJ, Yu B (2002) Climate sensitivity and response. *Clim Dyn* (in press)
- Boer GJ, McFarlane NA, Lazare M (1992) Greenhouse gas-induced climate change simulated with the CCC second-generation general circulation model. *J Clim* 5: 1045–1077
- Boer GJ, Flato G, Reader MC, Ramsden D (2000) A transient climate change simulation with greenhouse gas and aerosol forcing: experimental design and comparison with the instrumental record for the twentieth century. *Clim Dyn* 16: 405–425
- Boyle EA (1992) Cadmium and $\delta^{13}\text{C}$ paleochemical ocean distributions during the stage 2 glacial maximum. *Ann Rev Earth Planet Sci* 20: 245–287
- Boyle EA, Keigwin L (1982) Deep circulation of the North Atlantic over the last 200,000 years: geochemical evidence. *Science* 218: 784–787
- Boyle EA, Keigwin L (1987) North Atlantic thermohaline circulation during the past 20,000 years linked to high-latitude surface temperature. *Nature* 330: 35–40
- Broccoli AJ (2000) Tropical cooling at the Last Glacial Maximum: an atmosphere-mixed layer ocean model simulation. *J Clim* 13: 951–976
- Broecker WS (1986) Oxygen isotope constraints on surface ocean temperatures. *Quat Res* 26: 121–134
- Burke LH, Robinson D, Cooke D (1982) Reappraisal of sea-ice distribution in Atlantic and Pacific sectors of the Southern Ocean at 18,000 yr BP. *Nature* 299: 435–437
- Bush AB, Philander SG (1999) The climate of the Last Glacial Maximum: results from a coupled atmosphere–ocean general circulation model. *J Geophys Res* 24: 24,509–24,525
- CLIMAP (1976) The surface of the Ice-Age Earth. *Science* 191: 1131–1136
- CLIMAP (1981) Seasonal reconstructions of the Earth's surface at the last glacial maximum. *Geol Soc Am Map Chart Ser*, MC-36
- Colinvaux PA, De Oliveira PE, Moreno JE, Miller MC, Bush MB (1996) A long pollen record from lowland Amazonia: forest and cooling in glacial times. *Science* 274: 85–88
- Crowley TJ, Parkinson CL (1988) Late Pleistocene variations in Antarctic sea ice I: effects of orbital insolation changes. *Clim Dyn* 3: 85–91
- Crowley TJ, North GR (1991) *Paleoclimatology*. Oxford Monographs on Geology and Geophysics 18. Oxford University Press, New York
- Crowley TJ, Baum SK (1997) Effect of vegetation on an ice-age climate model simulation. *J Geophys Res* 102: 16,463–16,480
- Curry WB, Lohman (1982) Carbon isotope changes in benthic foraminifera from the western South Atlantic: reconstruction of glacial abyssal circulation patterns. *Quat Res* 18: 218–235
- Curry WB, Duplessy J-C, Labeyrie LD, Shackleton NJ (1988) Changes in distribution of $\delta^{13}\text{C}$ of deepwater ΣCO_2 between the last glaciation and the Holocene. *Paleoceanography* 3: 317–342
- DeAngelis M, Barkov NI, Petrov VN (1987) Aerosol concentrations over the last climatic cycle (160 kyr) from an Antarctic ice core. *Nature* 325: 318–321
- De Vernal A, Hillaire-Marcel C, Turon J-L, Matthiessen J (2000) Reconstruction of sea-surface temperature, salinity, and sea-ice cover in the northern North Atlantic during the last glacial maximum based on dinocyst assemblages. *Can J Earth Sci* 37: 725–750
- Duplessy J-C, Moyes J, Pujol C (1980) Deep water formation in the North Atlantic ocean during the last ice age. *Nature* 286: 476–482
- Duplessy J-C, Shackleton NJ, Fairbanks RG, Labeyrie L, Oppo D, Kallel N (1988) Deep water source variations during the last climatic cycle and their impact on the global deepwater circulation. *Paleoceanography* 3: 343–360
- Elderfield H, Ganssen G (2000) Past temperature and $\delta^{18}\text{O}$ of surface ocean waters inferred from foraminiferal Mg/Ca ratios. *Nature* 405: 442–445
- Fairbanks RG (1989) A 17,000-year glacio-eustatic sea level record: influence of glacial melting rates on the Younger Dryas event and deep-ocean circulation. *Nature* 342: 637–642
- Farrera I, Harrison SP, Prentice IC, Ramstein G, Guiot J, Bartlein PJ, Bonnefille R, Bush M, Cramer W, von Grafenstein U, Holmgren K, Hooghiemstra H, Hope G, Jolly D, Lauritzen S-E, Ono Y, Pinot S, Stute M, Yu G (1999) Tropical climates at the Last Glacial Maximum: a new synthesis of terrestrial paleoclimate data. I. Vegetation, lake-levels and geochemistry. *Clim Dyn* 15: 823–856
- Fichefet T, Hovine A, Duplessy J-C (1994) A model study of the Atlantic thermohaline circulation during the last glacial maximum. *Nature* 372: 252–255
- Flato GM, Hibler III WD (1992) Modelling pack ice as a cavitating fluid. *J Phys Oceanogr* 22: 626–651
- Flato GM, Boer GJ (2001) Warming asymmetry in climate change simulations. *Geophys Res Lett* 28: 195–198
- Flato GM, Boer GJ, Lee WG, McFarlane NA, Ramsden D, Reader MC, Weaver AJ (2000) The Canadian Centre Climate Modelling and Analysis global coupled model and its climate. *Clim Dyn* 16: 451–467
- Ganopolski A, Rahmstorf S, Petoukhov V, Claussen M (1998) Simulation of modern and glacial climates with a coupled global model of intermediate complexity. *Nature* 391: 351–356
- Gates WL (1976) Modelling the Ice-Age climate. *Science* 191: 1138–1144
- Gent PR, McWilliams JC (1990) Isopycnal mixing in ocean circulation models. *J Phys Oceanogr* 20: 150–155
- Greatbatch RJ, Fanning AF, Goulding AD, Levitus S (1991) A diagnosis of interpentadal circulation changes in the North Atlantic. *J Geophys Res* 96: 22,009–22,023
- Guilderson TP, Fairbanks RG, Rubenstone JL (1994) Tropical temperature variations since 20,000 years ago: modulating inter-hemispheric climate change. *Science* 263: 663–665
- Hall IR, McCave N, Shackleton NJ, Weedon GP, Harris SE (2001) Intensified deep Pacific inflow and ventilation in Pleistocene glacial times. *Nature* 412: 809–812
- Holland WR (1973) Baroclinic and topographic influences on the transport in western boundary currents. *Geophys Fluid Dyn* 4: 187–210

- Hansen J, Sato M, Ruedy R (1997) Radiative forcing and climate response. *J Geophys Res* 102: 6831–6864
- Harvey LD (1986) Computational efficiency and accuracy of methods for asynchronously coupling atmosphere–ocean climate models. Part II: testing with a seasonal cycle. *J Phys Oceanogr* 16: 11–24
- Hewitt CD, Broccoli AC, Mitchell JF, Stouffer RJ (2001) A coupled model study of the Last Glacial Maximum: was part of the North Atlantic relatively warm? *Geophys Res Lett* 28: 1571–1574
- Hughes CW, De Cuevas BA (2001) Why western boundary currents in realistic ocean are inviscid: a link between form stress and bottom pressure torques. *J Phys Oceanogr* 31: 2871–2885
- Janecek TR, Rea DK (1985) Quaternary fluctuations in the Northern Hemisphere trade winds and westerlies. *Quat Res* 24: 150–163
- Joussame S, Taylor KE (2000) The paleoclimate modeling inter-comparison project (PIMIP). In: Braconnot P (ed) *Proc third PIMIP Workshop*, Canada, pp 9–24
- Kim S-J, Flato GM, Boer GJ, McFarlane NA (2002) A coupled climate model simulation of the Last Glacial Maximum, Part 1: transient multi-decadal response. *Clim Dyn* 19: 515–537
- Kitoh A, Murakami S, Koide H (2001) A simulation of the Last Glacial Maximum with a coupled atmosphere–ocean GCM. *Geophys Res Lett* 28: 2221–2224
- Kohfeld KE, Harrison SP (2000) How well can we simulate past climates? Evaluating the models using global paleoenvironmental datasets. *Quat Sci Rev* 19: 321–346
- Kutzbach JE, Guetter P (1986) The influence of changing orbital parameters and surface boundary conditions on climate simulations for the past 18,000 years. *J Atmos Sci* 43: 1726–1738
- Ledbetter MT (1984) Bottom-current speed in the Vema Channel recorded by particle size of sediment fine-fraction. *Mar Geol* 58: 137–149
- Lynch-Stieglitz J, Curry WB, Slowey N (1999) Weaker Gulf Stream in the Florida Straits during the last glacial maximum. *Nature* 402: 644–648
- Manabe S, Bryan K (1969) Climate calculations with a combined ocean–atmosphere model. *J Atmos Sci* 26: 786–789
- Manabe S, Hahn DG (1977) Simulation of the tropical climate of an ice age. *J Geophys Res* 82: 3889–3911
- Manabe S, Broccoli AJ (1985) The influence of continental ice sheets on the climate of an ice age. *J Geophys Res* 90: 2167–2190
- Manabe S, Stouffer RJ (1988) Two stable equilibria of a coupled ocean–atmosphere model. *J Clim* 1: 841–866
- Manabe S, Stouffer RJ, Spelman MJ, Bryan K (1991) Transient responses of a coupled ocean–atmosphere model to gradual changes of atmospheric CO₂. Part I: annual mean response. *J Clim* 4: 785–818
- Martinez JJ, De Deckker P, Chivas AR (1997) New estimates for salinity changes in the Western Pacific Warm Pool during the last glacial maximum: oxygen-isotope evidence. *Mar Micropal* 32: 311–340
- McCulloch MT, Tudhope AW, East TM, Mortimer GE, Chappell J, Pillans B, Chivas AR, Omura A (1999) Coral record of equatorial sea-surface temperature during the penultimate deglaciation at Huon Peninsula. *Science* 283: 202–204
- McFarlane NA, Boer GJ, Blanchet J-P, Lazare M (1992) The Canadian Climate Centre second-generation general circulation model and its equilibrium climate. *J Clim* 5(10): 1013–1044
- Mix AC, Morey AE, Pisias G, Hostetler SW (1999) Foraminiferal faunal estimates of paleotemperature: circumventing the no-analog problem yields cool ice age tropics. *Paleoceanography* 14: 350–359
- Molina-Cruz A (1977) The relations of the Southern trade winds to upwelling processes during the last 75,000 years. *Quat Res* 8: 324–338
- Oppo DW, Fairbanks RG (1987) Variability in the deep and intermediate water circulation of the Atlantic Ocean during the past 25,000 years: Northern Hemisphere modulation of the Southern Ocean. *Earth Planet Sci Lett* 86: 1–15
- Oppo DW, Horowitz M (2000) Glacial deep water geochemistry: South Atlantic benthic foraminiferal Cd/Ca and $\delta^{13}\text{C}$ evidence. *Paleoceanography* 15: 147–160
- Oppo DW, Rosenthal Y (1994) Cd/Ca changes in deep Cape Basin core over the past 730,000 years: response of circumpolar deepwater variability to Northern Hemisphere ice sheet melting? *Paleoceanography* 9: 661–675
- Pacanowski RC, Dixon K, Rosati A (1993) The GFDL modular ocean model users guide. GFDL Ocean Group Tech Rep 2. Geophysical Fluid Dynamics Laboratory, Princeton, USA, pp 46
- Peltier WR (1994) Ice age paleotopography. *Science* 265: 195–201
- Petit JR, Briat M, Royer A (1981) Ice age aerosol content from East Antarctic ice core samples and past wind strength. *Nature* 293: 391–394
- Pierrehumbert RT (1999) Huascanan $\delta^{18}\text{O}$ as an indicator of tropical climate during the Last Glacial Maximum. *Geophys Res Lett* 26: 1345–1348
- Rind D, Peteet D (1985) Terrestrial conditions and the Last Glacial Maximum and CLIMAP sea surface temperature estimates: are they consistent? *Quat Res* 24: 1–22
- Rutberg RL, Hemming SR, Goldstein SL (2000) Reduced North Atlantic Deep Water flux to the glacial Southern Ocean inferred from neodymium isotope ratios. *Nature* 405: 935–938
- Sarnthein M, Tetzlaff G, Koopman B, Wolter K, Pflaumann U (1981) Glacial and interglacial wind regimes over the eastern subtropical Atlantic and northwest Africa. *Nature* 293: 193–196
- Sarnthein M, Winn K, Duplessy J-C, Fontugne MR (1988) Global variations of surface ocean productivity in low and mid latitudes: Influence on CO₂ reservoirs of the deep ocean and atmosphere during the last 21,000 years. *Paleoceanography* 3: 361–399
- Sarnthein M, Winn K, Jung SJA, Duplessy J-C, Labeyrie L, Erikenkuser H, Ganssen G (1994) Changes in east Atlantic deep water circulation over the last 30,000 years: eight time slice reconstructions. *Paleoceanography* 9: 209–269
- Sausen R, Voss R (1996) Techniques for asynchronous and periodically-synchronous coupling of atmosphere and ocean models, Part I: general strategy and application to the cyclostationary case. *Clim Dyn* 12: 313–323
- Schlesinger ME (1979) Discussion of “A global ocean–atmosphere model with seasonal variation for future studies of climate sensitivity”. *Dyn Atmos Oceans* 3: 427–432
- Schrag DP, Hampt G, Murray DW (1996) Pore fluid constraints on the temperature and oxygen isotopic composition of the glacial ocean. *Science* 272: 1930–1932
- Semtner AJ (1976) A model for thermodynamic growth of sea ice in numerical investigations of climate. *J Phys Oceanogr* 6: 379–389
- Sikes EL, Keigwin LD (1994) Equatorial Atlantic sea surface temperature for the last 30 kyr: a comparison of $U_{37}^{K'}$, $\delta^{18}\text{O}$ and foraminiferal assemblage temperature estimates. *Paleoceanography* 9: 31–45
- Stouffer RJ, Manabe S (1999) Response of a coupled ocean–atmosphere model to increasing atmospheric carbon dioxide: sensitivity to the rate of increase. *J Clim* 12: 2224–2237
- Street-Perrott FA, Marchand DS, Roberts N, Harrison SP (1989) Global lake-level variations from 18,000 years to 0 years ago: a paleoclimate analysis. US DOE/ER/60304-H1 TR046, US Department of Energy
- Stute M, Forster M, Frischkorn H, Serejo A, Clark JF, Schlosser P, Broecker WS, Bonani G (1995) Cooling of tropical Brazil (5 °C) during the Last Glacial Maximum. *Science* 269: 379–383
- Thompson LG, Mosley-Thompson E, Davis ME, Lin P-N, Henderson KA, Cole-Dai J, Bolzan JF, Liu K-B (1995) Late glacial stage and holocene tropical ice core records from Huascanan, Peru. *Science* 269: 46–50
- Voss R, Sausen R (1996) Techniques for asynchronous and periodically-synchronous coupling of atmosphere and ocean models, Part II: impact of variability. *Clim Dyn* 12: 605–614
- Voss R, Sausen R, Cubasch U (1998) Periodically synchronously coupled integrations with the atmosphere–ocean general model ECHAM3/LSG. *Clim Dyn* 14: 249–266

- Vettoretti G, Peltier WR, McFarlane NA (2000) Global water balance and atmospheric water vapour transport at last glacial maximum: climate simulations with the Canadian Climate Centre for Modelling and Analysis atmospheric general circulation model. *Can J Earth Sci* 37: 695–723
- Weaver AJ, Eby M, Fanning AF, Wiebe EC (1998) Simulated influence of carbon dioxide, orbital forcing and ice sheets on the climate of the Last Glacial Maximum. *Nature* 394: 847–853
- Webster PJ, Streten NA (1978) Late Quaternary ice age climates of tropical Australasia: interpretation and reconstructions. *Quat Res* 10: 279–309
- Weinelt M, Sarnthein M, Pflaumann U, Schulz H, Jung S, Erlenleuser H (1996) Ice-free Nordic Seas during the Last Glacial Maximum? Potential sites of deepwater formation. *Paleoclimate* 1–4: 283–309
- Weyhenmeyer CE, Burns SJ, Waber NH, Aeschbach-Hertig W, Kipfer R, Loosli HH, Matter A (2000) Cool glacial temperature and changes in moisture source recorded in Oman groundwaters. *Science* 287: 842–845
- Wyputta U, McAvaney BJ (2001) Influence of vegetation changes during the Last Glacial Maximum using BMRC atmospheric general circulation model. *Clim Dyn* 17: 923–932
- Yu B, Boer GJ (2002) The roles of radiation and dynamical processes in the El Niño-like response to global warming. *Clim Dyn* 19: 539–553
- Yu E-F, Francois R, Bacon P (1996) Similar rates of modern and last-glacial ocean thermohaline circulation inferred from radiochemical data. *Nature* 379: 689–694